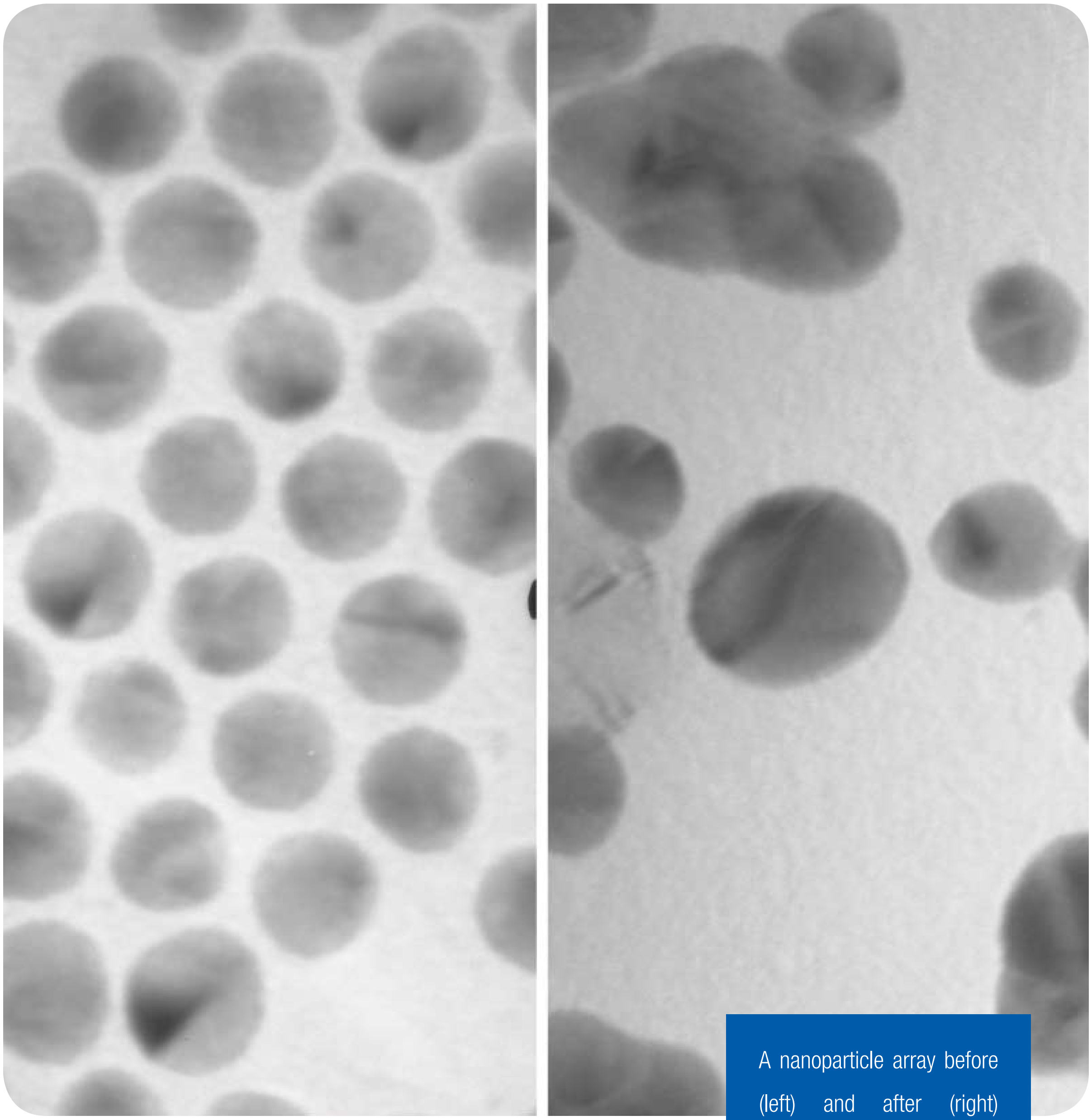

A nanoparticle array before (left) and after (right) heat treatment to induce particle sintering. Image by Thompson group.

MOLECULAR AND NANOTECHNOLOGY

TABLE OF CONTENTS

Nanostructured Origami™ Theory

P.S. Stellman, G. Barbastathis

Sponsorship: ISN, MARCO IFC

The Nanostructured Origami method [1] fabricates 3D devices first by patterning nanostructures (electronic, optical, mechanical, etc.) onto a 2D substrate, then by folding segments along pre-defined creases until the final design is obtained. This approach allows almost arbitrary 3D nanostructured systems to be fabricated using 2D nano-patterning tools exclusively.

We present two approaches to the kinematic and dynamic modeling of folding origami structures. The first approach addresses the kinematics of unfolding single-vertex origami structures. First, a unit positive "charge" is assigned to the creases of the structure in its folded state. Thus, each configuration of the structure as it unfolds can be assigned a value of electrostatic (Coulomb) energy [2]. Because of repulsion between the positive charges, the structure will unfold if its energy is allowed to decrease. We obtain the desired unfolding trajectory by numerical minimization using the steepest descent algorithm. If energy minimization can be carried out all the way to the completely unfolded state, we are simultaneously guaranteed the absence of collisions for the determined path. The electrostatic potential predicts the correct kinematics. However, this prediction is not physically realistic, and thus it does not give the correct dynamics of unfolding. The actual folding path is obtained by simply reversing the unfolding trajectories.

The second method achieves dynamic modeling of folding multi-segment (accordion style) origami structures. The actuation method for folding the segments uses a thin, stressed metal layer that is deposited as a hinge on a relatively stress-free structural layer. The strain energy induced by the internal reaction in the curling hinge is defined as a function of rotation angle, and the minimization of this potential energy results in the trajectory of the structure and its dynamic behavior. A computationally efficient collision-detection algorithm has also been implemented to check for self-intersections. Based on the trajectory and the collision-detection algorithm, we can iteratively design the actuation sequence for arbitrary accordion foldings.

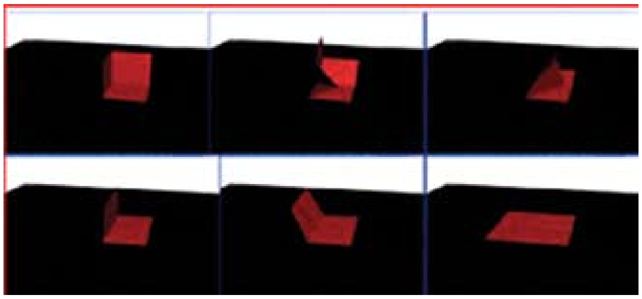

Figure 1: Kinematics of a single vertex origami (corner cube) using charge method.

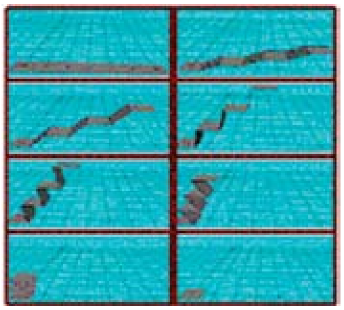

Figure 2: Dynamics of accordion style origami.

REFERENCES:

[1] Jurga, S.M., "3D Micro- and Nano-manufacturing via Folding of 2D Membranes," Massachusetts Institute of Technology Department of Mechanical Engineering, Cambridge, MA, Annual Report, p. 130, 2003.

[2] Cantarella, J.H., E.D. Demaine, H.N. Iben, J.F. O'Brien, "An Energy-driven Approach to Linkage Unfolding," *Twentieth Annual ACM Symposium on Computational Geometry,* Brooklyn, NY, pp.134-143, Jun. 2004.

Alignment Techniques for the Nanostructured Origami™ 3D Fabrication and Assembly Process

H.J. In, A. Nichol, W. Arora, H. Smith, G. Barbastathis

Sponsorship: MARCO IFC, ISN, NSF SGER

The Nanostructured Origami™ 3D Fabrication and Assembly Process enables the fabrication of nanostructured, 3D devices through the folding of micro- and nano-patterned membranes [1]. For a number of applications, such as electrochemical energy storage devices and 3D photonic crystals [2], a simple stacking-type folding is required. For such a folding scheme, lateral alignment among folded layers is crucial. We have folded SU-8 membranes with less than 1 µm lateral alignment error using patterned pyramids and corresponding square openings that couple during the assembly process. The pyramids are formed first by filling in KOH-etched trenches in the silicon with SU-8, then by etching away the silicon in a XeF_2 -etch. As the top SU-8 layer is folded on top of the bottom layer (Figure 1), the square openings fit precisely over the pyramids, thereby providing lateral alignment as well as vertical spacing between layers. The scanning electron microscopy (SEM) image in Figure 2 shows the centered tip of the pyramid in relation to the square opening.

Lateral alignment precision must be on the order of 10 nm for devices such as photonic crystals and 3D integrated circuits. Other possible alignment techniques include alignment via hydrophobic/hydrophilic surfaces and using electrostatic or magnetic forces. These alignment structures are patterned via high precision lithography techniques, such as e-beam lithography, and the alignment system must produce sufficient forces to overcome other factors at this size scale, such as van der Waal's forces and surface tension. Lateral alignment is further improved by "elastic averaging," which occurs when a large array of alignment mechanisms work in parallel for greater alignment precision. We are pursuing a variety of methods to analyze the precision of the passive and active alignment schemes as well. The first method is to pattern visual markings on the membranes, such as cross-hatches and moiré patterns, that show the post-assembly lateral alignment under an optical microscope or SEM. Furthermore, device functionality will serve as a precise measure for alignment (e.g., a photonic crystal's band properties).

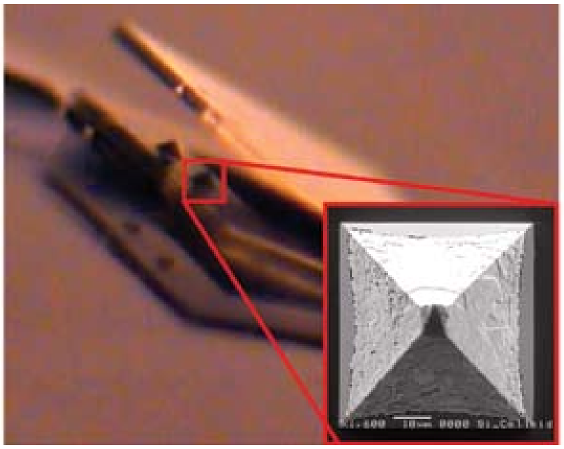

Figure 1: Partially folded SU-8 device with pyramid-shaped alignment features.

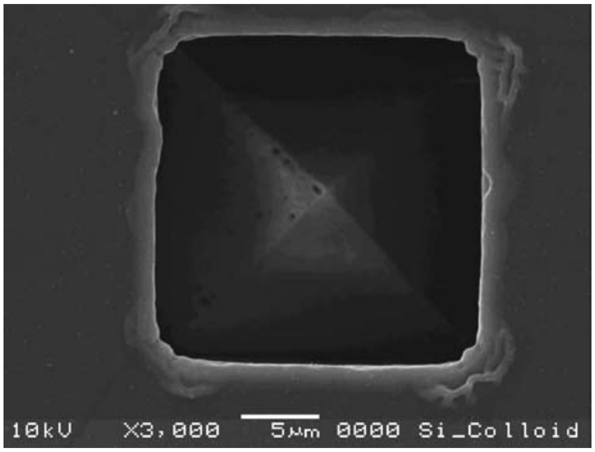

Figure 2: SEM image of a square opening fitted over a pyramid. Location of pyramid tip indicates sub-micron alignment.

REFERENCES:

[1] In, H.J., W. Arora, T. Buchner, S.M. Jurga, H.I. Smith, G. Barbastathis, "The Nanostructured Origami™ 3D Fabrication and Assembly Process for nanomanufacturing," *Fourth IEEE Conference on Nanotechnology,* Munich, Germany, pp. 358-360, August 2004.

[2] In, H.J., W. J. Arora, S. Kumar, Y. Shao-Horn, H.I. Smith, G. Barbastathis, "Fabrication of 3D Nanostructures via Nanostructured Origami™ Process," *Second International Symposium on Nanomanufacturing*, Daejon, Korea, November 2004.

Nanostructured Origami™ 3D Fabrication and Assembly of Electrochemical Energy Storage Devices

H.J. In, S. Kumar, Y. Shao-Horn, G. Barbastathis

Sponsorship: MARCO IFC, ISN, NSF SGER

In the Nanostructured Origami™ 3D Fabrication and Assembly Process, 3D nanostructured devices can be made using exclusively 2D micro- and nano-fabrication tools [1]. The origami approach consists of first patterning 2D nanostructured membranes, then folding them to obtain the desired 3D shape. The fact that nanostructured surfaces can be oriented in any direction makes the Nanostructured Origami™ Process ideal for fabricating electrochemical energy storage devices, such as supercapacitors, [2] where it is desirable to have two nanostructured surfaces facing each other. In addition, because the origami method can be integrated with most existing fabrication processes, on-chip power supply integration becomes possible. Figure 1 shows the process flow for an origami supercapacitor. SU-8 serves as the structural material, and carbon paint deposited on top of gold acts as the electrode material. While the carbon paint itself is highly porous and can be considered a nanostructure, the gold surface underneath is patterned with small pyramids to further increase the total surface area (Figure 2). Initial electrochemical testing of the supercapacitor device shows that a large capacitance can be obtained from a device that takes up no more than 500 μm x 500 μm x 50 μm. Future work will include testing of multi-layered electrochemical devices that maintain a small areal footprint despite a very large surface area.

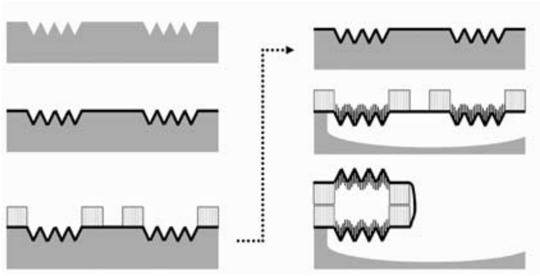

Figure 1: Process flow for SU-8 supercapacitors (gray = silicon, black = gold, light stripe = SU-8, dark stripe = carbon paint).

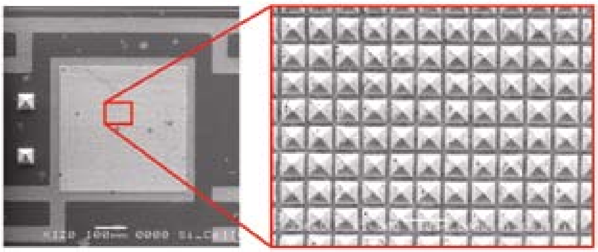

Figure 2: Scanning electron microscope image of 3 μm square pyramids that serve to increase the overall surface area of the electrode.

REFERENCES:

[1] In, H.J., W. Arora, T. Buchner, S.M. Jurga, H.I. Smith, G. Barbastathis, "The Nanostructured Origami™ 3D Fabrication and Assembly Process for nanomanufacturing," *Fourth IEEE Conference on Nanotechnology,* Munich, Germany, pp. 358-360, August 2004.

[2] In, H.J., W.J. Arora, S. Kumar, Y. Shao-Horn, H.I. Smith, G. Barbastathis, "Fabrication of 3D nanostructures via Nanostructured Origami™ Process," *Second International Symposium on Nanomanufacturing*, Daejeon, Korea, November 2004.

Stress Actuation Method for Folding Nanostructured Origami

W.J. Arora, H. Smith, G. Barbastathis

Sponsorship: MARCO IFC, DARPA, ISN

Nanostructured Origami describes a new idea for manufacturing 3D nanostructures on a silicon wafer. Nanometer-scale structures are best fabricated with various 2D lithography techniques. This project addresses the problem of how to build 3D structures using only 2D lithography. The general method of the Nanostructured Origami approach involves three steps: (1) lithographically define micrometer-scale membranes and hinges; (2) lithographically pattern nanostructures on these membranes; and (3) release the membranes and actuate the hinges to fold into a 3D shape.

We have developed a process to fold thin membranes of silicon nitride using stressed chromium hinges. The chromium is deposited with high tensile residual stress by vacuum evaporation, and the membranes are subsequently released with a KOH underetch. As the membrane is released, the chromium hinges self-actuate due to their stress. Figures 1 and 2 show experimental results of the folding process. For a given value of residual stress in the chromium, the hinge will curl with a predictable radius [1]. Therefore, the angle to which the membrane folds is proportional to the length of the chromium hinge (Figure 1). We have also demonstrated 180° folds (not shown).

Our current work is focused on nano-patterning the silicon nitride membranes with electron-beam lithography prior to releasing them. In addition, we plan to reduce the hinge radius of curvature by selectively thinning the silicon nitride at the hinge area. With these improvements, Nanostructured Origami becomes a tool well-suited for the fabrication of 3D nano-devices, including 3D photonic crystals and 3D ICs.

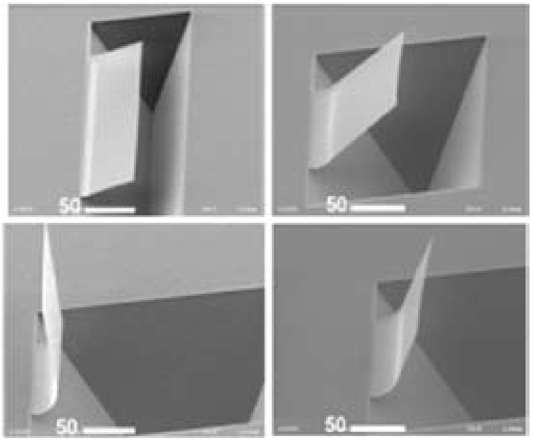

Figure 1: Clockwise from the top left, the lengths of the chromium hinges were (in µm):12, 27, 42, and 54. The angles at which they folded are approximately (in degrees) 20, 45, 70, 90.

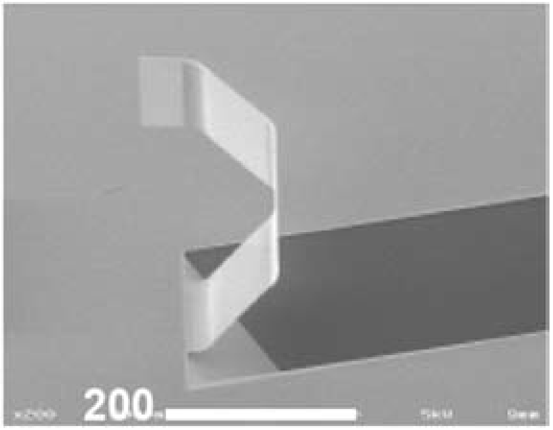

Figure 2: A device with four identical hinges.

REFERENCES:

[1] Arora, W.J., H.J. In, T. Buchner, H.I. Smith, G. Barbastathis, "Nanostructured Origami™ 3D Fabrication and Assembly Process Using Strain Actuated Folding," *Second International Symposium on Nanomanufacturing*, Daejeon, Korea, November 2004.

Mechanical Deformation of Neutrophils into Narrow Channels Induces Pseudopod Projection and Changes in Biomechanical Properties

B. Yap, R.D. Kamm

Sponsorship: National Heart, Lung, and Blood Institute (Program Project Grant)

Neutrophils traversing the pulmonary microcirculation are subjected to mechanical stimulation during their deformation into narrow capillaries. To better understand the time-dependant changes caused by this mechanical stimulus, we used microfabrication techniques to construct an *in-vitro* poly-dimethyl-siloxane (PDMS) system with dimensions comparable to the pulmonary capillaries. Because PDMS is optically transparent, it enabled direct observation of the neutrophil morphology, and simultaneously allowed us to employ the technique of multiple-particle-tracking microrheology to directly measure the viscoelastic properties of the cell. Above a threshold stimulus, mechanical deformation resulted in neutrophil activation with pseudopod projection. The activation time was inversely correlated to the rate of mechanical deformation experienced by the neutrophils. A reduction in shear moduli was observed within seconds after the onset of the mechanical stimulus, suggesting a sudden disruption of the neutrophil cytoskeleton when subjected to mechanical deformation. However, the magnitude of the reduction in moduli was independent of the degree of deformation. Recovery to nearly the initial values of viscoelastic moduli occurred within one minute. These observations confirm that mechanical deformation of neutrophils, similar to conditions encountered in the pulmonary capillaries is not a passive event; rather, it is capable of activating the neutrophils and enhancing their migratory tendencies.

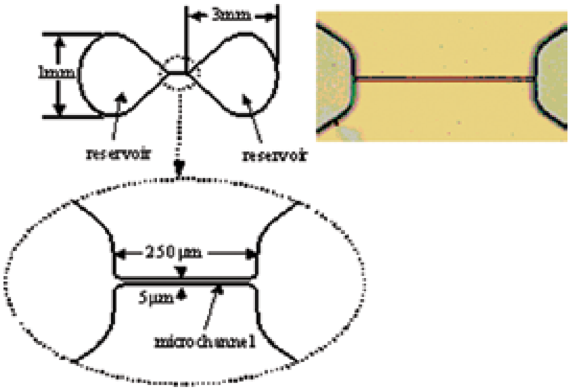

Figure 1: (Left) Schematic showing design of the PDMS microchannel and its connecting reservoirs. The microchannel section is enlarged to highlight the channel geometry, which has dimensions comparable to those of pulmonary capillaries. The microchannel height is about 1.5-2.5. Diagrams are not drawn to scale. (Right) Image of the microchannel as observed under a microscope.

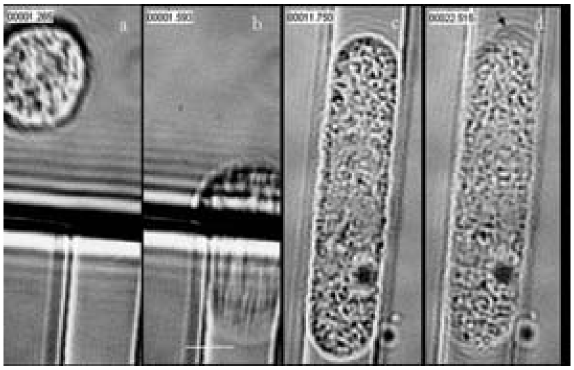

Figure 2: Image sequence showing a neutrophil flowing towards the microchannel entrance [panel (a)], the cell undergoing deformation [panel (b)], and subsequently, the neutrophil being trapped in the channel [panel (c)]. After some time, the cell can be seen to form pseudopod projection [panel (d)]. Arrow in panel (d) points to the location at the trailing edge of the cell where pseudopod protrusion was first seen. The granules in the cell were tracked to obtain the viscoelastic properties of the cytoplasm. Scale bar, 5.

REFERENCES:

[1] Yap, B., D. Kamm, "Mechanical Deformation of Neutrophils into Narrow Channels Induces Pseudopod Projection and Changes in Biomechanical Properties," *Journal of Applied Physiology*, vol. 98, no. 5, pp.1930-1939, May 2005.

Field Ionization Array Micro-Gas Analyzer

L.F. Velásquez–García, L.Y. Chen, B. Andeoti, A.I. Akinwande

Sponsorship: DARPA

The Micro Gas Analyzer (MGA) project aims to develop the technology for real-time sensors intended for chemical warfare. The device is composed of four micro-fabricated subsystems: 1) an ionizer; 2) a mass filter based on a quadrupole [1]; 3) a species sensor based on a resonator [2]; and 4) a pump [3]. We are developing a field ionizer array based on gated CNTs. We plan to use arrays of CNTs because of their small radii, high aspect ratio, and gate proximity to ensure high fields at low voltage. State-of-the-art ionizers use electron impact ionization (thermionic cathodes), incurring in excessive power consumption, low current, current density, ionization efficiency, and short lifetime. Each of the proposed ionizer arrays - the impact and field - offer distinct advantages. The electron impact ionizer and field ionizer arrays both are more efficient and consume less power than thermionic cathodes, and variation of gate voltage in each improves specificity. The field ionizer, however, is based on the concept of electron tunneling (electrons tunnel in the outer shell of the molecule, due to the presence of high electric fields). Because of this, the field ionizer is able to soft-ionize species, thus achieving molecule ionization. The reliability and device lifespan of the field-tunneling ionizer is increased by biasing CNTs to the highest potential in the circuit, thus making it unlikely for ionized molecules to back-stream. In the case of the electron impact ionizer, the reliability and lifespan of the ionizer is improved by using a double gate.

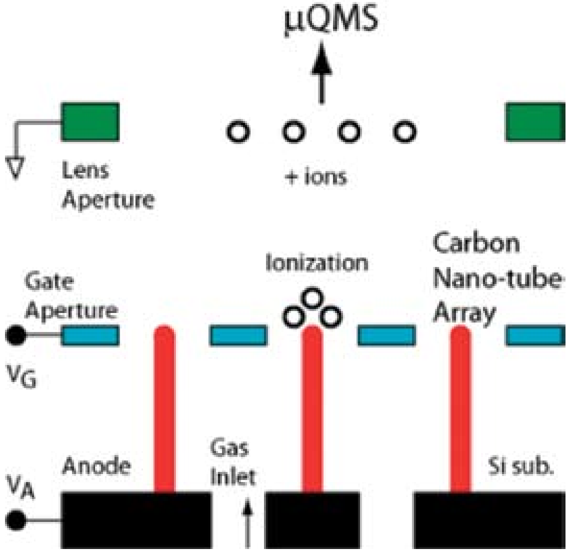

Figure 1: Schematic of a field ionizer array based on electron tunneling from the actual molecule to be ionized. Neutral molecules will lose an external electron if they get close enough to the CNT tip. The positive- biased CNT will repel the ion.

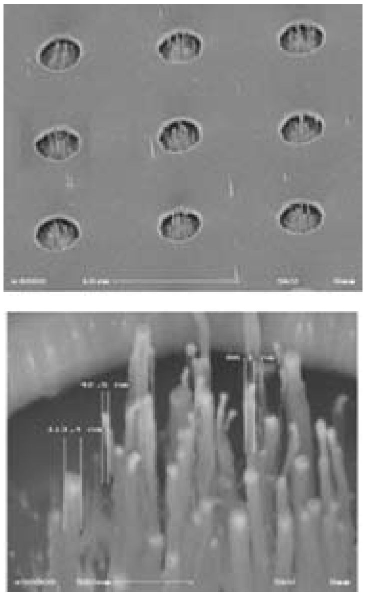

Figure 2: A single gated CNT array grown at MIT. The gate is made of poly-SSi, the insulator is thermal SiO_2. The CNT seed was Fe.

REFERENCES:

[1] Syms, R.R.A. *et al.*, "Design of a Microengineered Electrostatic Quadrupole Lens," *IEEE Transactions on Electron Devices*, vol. 45, no. 11, p. 2304, 1988.

[2] Riehl, P.S. *et al.,* "Electrostatic Charge and Field Sensors Based on Micromechanical Resonators," *Journal of Micromechanical Systems*, vol. 12, no. 5, p. 577, 2003.

[3] Li, H.Q. *et al.*, "A High-frequency High-flow Rate Piezoelectrically Driven Mems Micropump," *IEEE Solid State Sensors and Actuators Workshop*, Hilton Head, SC, June 2000.

Fast Separation of Biomolecules in a Nanofilter Array Chip

J. Fu, J. Han

Sponsorship: NSF-CTS, MIT Lincoln Laboratory

We report here the first microfabricated nanofilter array chip that can size-fractionate SDS-protein complexes and small dsDNA molecules based on the Ogston sieving mechanism [1] without using sieving matrices. Nanofilter arrays with a gap size of 40-180 nm were fabricated and characterized. Complete separation of SDS-protein complexes and small DNA molecules were achieved in several minutes with a separation length of 5 mm. The separation efficiency of the miniature nanofilter array chip is comparable to current state of the art systems (i.e., capillary gel electrophoresis). Our work here is the first direct experimental confirmation of Ogston sieving in a well-defined, regular nanopore system, and the nanofilter array chip is the first microfabricated, regular sieving system that can size-separate small biomolecules, such as proteins.

The nanofilter array chip is chemically and mechanically robust, and can be used over a long period without degradation of its characteristics. The nanofilter array chip allows the use of different buffer systems, and this opens up possibilities for integrating different biomolecule sensors and separation and reaction chambers in one single chip, without the concern of sieving matrix crosstalk and contamination. Therefore, the nanofilter array chip presented here is an important milestone toward a truly integrated proteomic sample-preparation microsystem that includes fully-integrated multiple separation and purification steps.

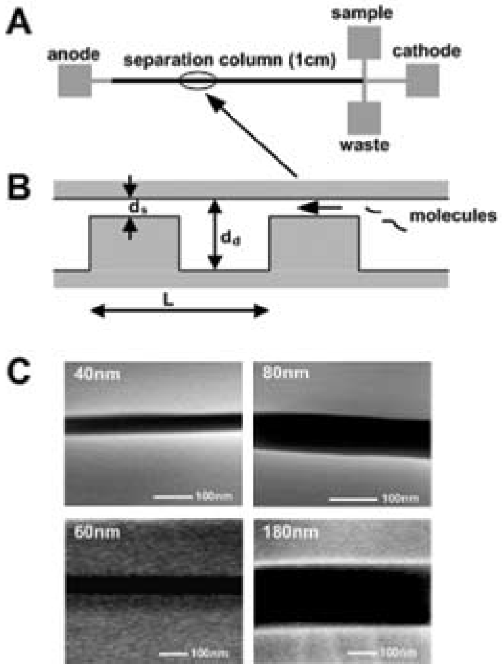

Figure 1: (A) Layout of the nanofilter array chip. (B) Schematic diagram of the nanofilter array. (C) Scanning electron microscope images of thin regions with different depths.

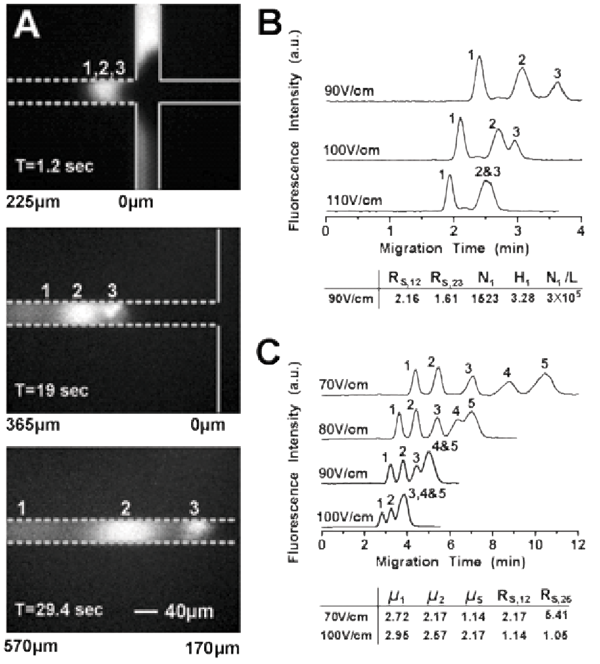

	$R_{S,12}$	$R_{S,23}$	N_1	H_1	N_1/L
90V/cm	2.16	1.61	1623	3.28	3×10^5

	μ_1	μ_2	μ_5	$R_{S,12}$	$R_{S,25}$
70V/cm	2.72	2.17	1.14	2.17	5.41
100V/cm	2.95	2.57	2.17	1.14	1.05

Figure 2: Fast separation of SDS-protein complexes (A) and (B) 1: cholera toxin subunit B, 11.4kDa; 2: lectin phytohemagglutinin-L, 120kDa; 3: low density human lipoprotein, 179kDa and small dsDNA molecules (C, PBR marker, 1: 50bp, 2: 150bp, 3: 300bp, 4:500bp, 5:766bp).

REFERENCES:

[1] Ogston, A.G., "The Spaces in a Uniform Random Suspension of Fibers," *Trans. Faraday Soc.*, vol. 54, pp. 1754-1757, 1958.

Fabrication and Characterization of Nanofluidic Channels for Studying Molecular Dynamics in Confined Environments

P. Mao, J. Han, M. Previte, P.T.C. So, A.G. Balducci, P.S. Doyle

Sponsorship: MIT Lincoln Lab, NSF NSE and CAREER program

Hindered transport of macromolecules in liquid-filled pores is important to biological membrane processes associated with cell biology and medical physiology, chromatography, separation, and heterogeneous catalysis [1]. It is highly desirable to conduct well-controlled, model-based studies of molecular and fluidic transport process in a confined space. Compared to nanoporous track-etched membranes, micromachined nanofluidic structures offer unique advantages, including well-controlled physical and chemical properties, compatibility with various single molecule detection (SMD) methods, and easy integration to μTAS [2]. We characterized glass-glass and glass-Si bonding processes for the fabrication of nanofluidic channels as thin as 20 nm (Figure 1). We demonstrated that glass-glass nanofluidic channels as thin as 25 nm, with a high aspect ratio of 2000 (width to depth), can be achieved with this glass-glass bonding technique. We also found that silicon-glass nanofluidic channels, as thin as 20 nm, with an aspect ratio of 250, can be reliably obtained with the anodic bonding technique. Cross-sectional scanning electron microscopy (SEM) analysis after bonding was performed to prove that there is no significant change in the depth of the nanofluidic channels due to anodic bonding and glass-glass fusion bonding processes [3]. We examined the conformation and diffusion of a single λ-DNA molecule confined in a slit glass nanochannel using epifluorescence video microscopy (Figure 2(A)) [4]. The diffusivity is characterized as a function of the degree of chain confinement (depth of the channel). In addition, the effects of spatial confinement and surface boundary layer on the diffusivity of small biomolecules within a nanochannel are being investigated by two-photon fluorescence correlation spectroscopy (FCS), shown in Figure 2(B). The potential impact of this research would be significant, both scientifically and technologically, by offering a better understanding of molecular diffusion and transport in confined environments, as well as generating new concepts of molecular sorting and manipulation technology.

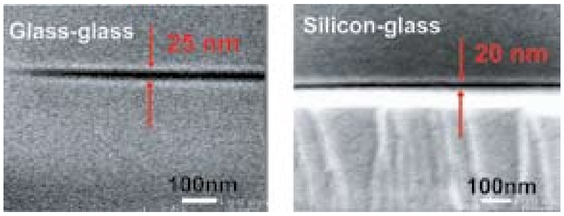

Figure 1: Cross-sectional SEM images of the 25 nm glass-glass channel (A) and 20 nm silicon-glass channel (B).

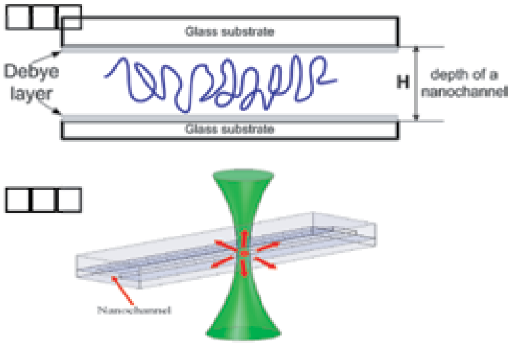

Figure 2: (A) Schematic diagram of a large DNA molecule confined to a slit glass nanochannel with a depth of H. (B) Schematic diagram of detecting single, small molecules by two-photo FCS in a slit nanochannel with vertical confinement.

REFERENCES:

[1] Deen, W.M., “Hindered Transport of Large Molecules in Liquid-filled Pores,” *AIChE Journal*, vol. 33, pp. 1409-1425, 1987.

[2] Han, J., “Nanofluidics,” in *Introduction to Nanoscale Science and Technology*, eds. M. DiVentra, S. Evoy, and J.R. Heflin (Norwalt: Kluwer Academic Publishers, 2004).

[3] Mao, P., “Fabrication and Characterization of Nanofluidic Channels for Studying Molecular Dynamics in Confined Environments,” Massachusetts Institute of Technology, Cambridge, MA, Mechanical Engineering Annual Report, 2005.

[4] Chen, Y.-L., M.D. Graham, J.J.D. Pablo, G.C. Randall, M. Gupta, P.S. Doyle, “Conformation and Dynamics of Single DNA Molecules in Parallel-plate Slit Microchannels,” *Physical Review E: Statistical, Nonlinear, and Soft Matter Physics*, vol. 70, no. 6, pp. 060901: 1-4, 2004.

Millionfold Biomolecule Pre-Concentration Using Nano-fluidic Filters

Y.-C. Wang, J. Han

Sponsorship: NSF, MIT Lincoln Lab

In all biomolecule-sensing technologies, detection becomes increasingly difficult or impossible when the analyte concentration is lower than a certain level (the detection limit). However, in complex blood-serum samples, most of the important biomolecule markers are available only in trace amounts (fM to nM). Therefore, the detection (or identification) of these markers after pre-fractionation and separation is extremely difficult. To solve this problem, numerous efforts have been made to develop a pre-concentration process before or after separation. So far, the single pre-concentration method with the highest concentration factor among all the strategies is micellar electrokinetic sweeping, which can achieve a concentration factor of 500-to 7000-fold [1,2].

Here, we present a novel way to achieve rapid pre-concentration for a charged biomolecule that can achieve an up to 10 millionfold sample pre-concentration within 30 minutes. Ionic charge separation will happen once the electrical field is applied across the nanofilter. It has been reported that a flow several times stronger than general electroosmotic flow, caused by induced-charge layer, will present with confined geometry [3,4]. As a consequence, a barrier that can trap both positively and negatively charged molecules is formed by extending the Debye layer (non-equilibrium charge polarization) into the microfluidic channel with a stronger carrier flow. This device can concentrate a sample without a complex buffer concentration variation (such as in electrokinetic focusing), any additional additive (such as SDS in micellar sweep techniques), and/or any other complex structure that will make the downstream analysis difficult. Because of the device's simple structure, various integrations and applications are possible, including sample pre-concentration for advanced blood proteome analysis, sample injection for microchip electrophoresis/chromatography, and environmental trace analysis.

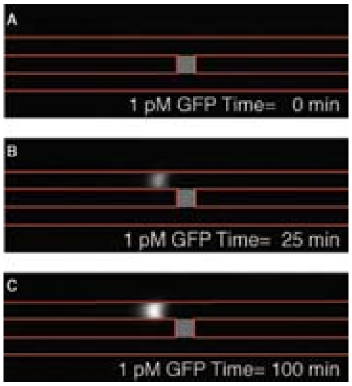

Figure: 1: Pre-concentration phenomena for 100 minutes, starting from highly diluted 33 pM (10-12M) GFP solution. The detection condition barely detects the 33 μM GFP concentration, which means at 25 minutes or later, the concentration of the plug exceeds 1 μM. Voltage applied across top-down channel is 10 volts, while 4 volts along the top channel (pictures were taken by CCD camera with 1 second exposure).

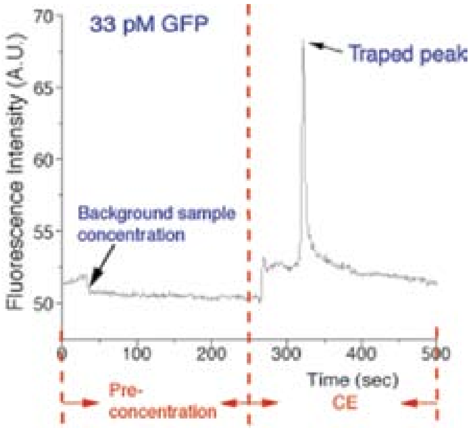

Figure: 2: Picture showing the electrokinetic capture/release profiles. After 250 seconds, the waster channel was floated to perform an EOF--driven CE in the top channel. Shown between 300 and 350 seconds is the releasing of captured proteins.

REFERENCES:

[1] Quirion, J.P., S. Terabe, "Exceeding 5000-fold Concentration of Dilute Analytes in Micellar Electrokinetic Chromatography," *Science*, vol. 282, no. 5388, pp. 465-468, October 1998.

[2] Molina, M., M. Silva, "Micellar Electrokinetic Chromatography: Current Developments and Future," *Electrophoresis*, vol. 23, no. 23-23, pp. 3907-3921, December 2002.

[3] Leinweber, F.C., U. Tallarek, "Nonequilibrium Electrokinetic Effects in Beds of ion-permselective Particles," *Langmuir*, vol. 20, no. 26, pp. 11637-11648, September 2004.

[4] Bazant, M.Z., T.M. Squires, "Induced-charge Electrokinetic Phenomena: Theory and Microfluidic Applications," *Physical Review Letters*, vol. 92, no. 6, p. 066101, February 2004.

A Nanoscanning Platform for Biological Assays

S. Kim, C. Muller-Falcke, S. Gouda, S.-G. Kim (Peter So group)

Sponsorship: IMC

Despite its success as an imaging tool for nanostructures, the existing atomic force microscopy (AFM) system does not reflect functionalities needed for biological applications well. One major problem with existing AFMs is slow imaging speed. Another problem is poor compatibility of the tip to the soft surface of biological specimens [1]. A nanoscanning platform is being developed at the Micro & Nano Systems Laboratory (MNSL). It has an in-plane structure with variable stiffness and a carbon nanotube tip (MWNT). Because of their superior mechanical and chemical properties, CNTs not only are ideal candidates for AFM tips, but they also are ideal for tip-enhanced raman spectroscopy (TERS). The variable-stiffness AFM can work as a tool for imaging and for placing the tip at the sub-nanometer proximity to a soft molecular-scale biological sample to enhance the Raman signals. The metal-coated CNT, or CNT filled with silver, gold or copper, which has a small diameter tip and high aspect ratio, is ideal for TERS. It is expected that the CNTs' plasmonic behavior with photons and the variable stiffness of the in-plane probe can further enhance Raman signals, thereby providing a high-enough sensitivity for the imaging of single molecular structures, such as proteins.

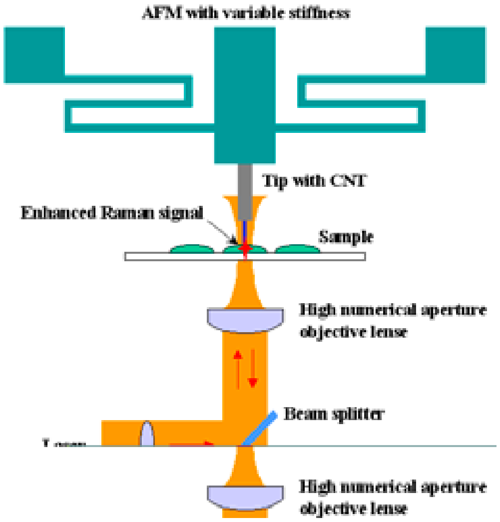

Figure 1: Schematic of TERS using an AFM with a CNT tip.

REFERENCES:

[1] Mueller-Falcke, C., S.D. Gouda, S. Kim, S.-G. Kim, "A Nano-scanning Platform for Bio-engineering," submitted to *The International Conference of Bio-Nano-Informatics (BNI) Fusion*, Marina del Rey, CA, July 20-22, 2005.

Microfluidic Synthesis and Surface Engineering of Colloidal Nanoparticles

S.A. Khan, A. Günther, F. Trachsel, M.A. Schmidt, K.F. Jensen

Sponsorship: Microchemical Systems Technology Center

Metal oxide colloidal particles such as silica (SiO_2) and titania (TiO_2) have many diverse applications ranging from optical displays, catalysis, pigments, and photonic band-gap materials to immunological assays and health-care products. There has also been considerable research interest over the last decade in fabricating core-shell materials with tailored optical, structural, and surface properties. Core-shell particles such as titania-coated silica often exhibit improved physical and chemical properties over their single-component counterparts, and hence, are potentially useful over a broader range of applications. Newer methods of engineering such materials with controlled precision are required to overcome the difficulties with conventional production techniques, which are limited to multi-step batch processes. We have developed microfluidic routes for synthesis, separation, and surface modification of colloidal silica and titania particles. The two chief advantages of a microfluidic particle-engineering platform are: (1) precise control over reactant addition; and (2) mixing and continuous operation. Figure 1 shows a microfluidic chemical reactor for the continuous synthesis of colloidal silica particles [1]. We have also developed a microfluidic device for the electrophoretic separation of charged colloidal particles [2]. Figure 2(a) is a scanning electron micrograph of silica particles synthesized in the micro-reactor of Figure 1, operated in segmented gas-liquid flow mode. Figure 2(b) shows a silica nanoparticle coated with a thick shell of titania. Our ultimate goal is to enable continuous, multi-step colloid processing, with applications including synthesis and surface modification with biological macro-molecules or optical coatings.

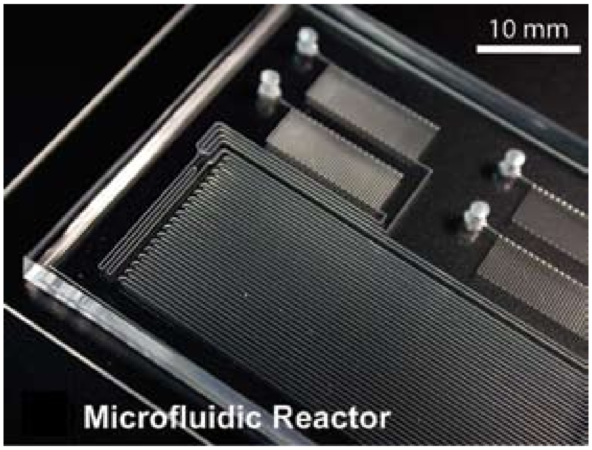

Figure 1: Microfluidic reactor for synthesis of colloidal silica, fabricated in PDMS.

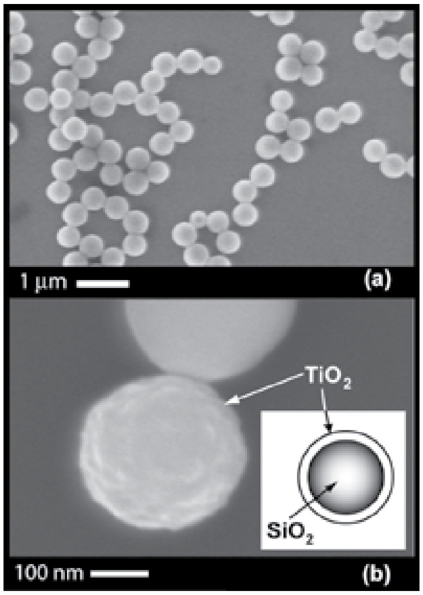

Figure 2: (a) Silica synthesized in micro-reactor and (b) titania-coated silica.

REFERENCES:

[1] Khan, S.A., A. Guenther, M.A. Schmidt, K.F. Jensen, "Microfluidic Synthesis of Colloidal Silica," Langmuir, vol. 20, pp. 8604-8611, 2004.
[2] Khan, S.A., A. Günther, F. Trachsel, M.A. Schmidt, K.F. Jensen, "Microfluidics for Colloids Processing," Eighth International Conference on Miniaturized Systems for Chemistry and Life Sciences, Malmö, Sweden, pp. 414-416, September 2004.

Microreactors for Synthesis of Quantum Dots

B.K.H. Yen, A. Günther, M.A. Schmidt, M.G. Bawendi, K.F. Jensen

Sponsorship: Microchemical Systems Technology Center, NSF, ISN

We have fabricated a gas-liquid segmented flow reactor with multiple temperature zones for the synthesis of quantum dots (QDs). In contrast to the single-phase flow approach, the segmented flow approach enables rapid mixing and narrow residence time distributions – factors that have a strong influence on the ultimate QD size distribution. The silicon-glass reactor accommodates one reaction channel approximately one meter in length (hydraulic diameter ~400 μm), and two shallow side channels for collecting reaction aliquots (Figure 1). Two temperature zones are maintained, a heated reaction region (260°C) and a cooled quenching region (<70°C). As a model system, CdSe quantum dots with high quantum yields and low polydispersity are prepared using the reactor. Cadmium and selenium precursor solutions are delivered separately into the heated section. An inert gas stream is introduced further downstream to form a segmented gas-liquid flow, thereby rapidly mixing the precursors and initiating the reaction. The reaction is stopped when the fluids enter the cooled outlet region of the device. Under conditions for a typical synthesis, the gas and liquid segments are very uniform, and the QDs produced possess narrow size distributions, as indicated by the narrow line-widths in the photoluminescence spectra (Figure 2). The enhanced mixing and narrow residence time distributions offered by the segmented flow approach are generally desirable for nanoparticle synthesis, and we intend to apply the reactor to the preparation of other material systems.

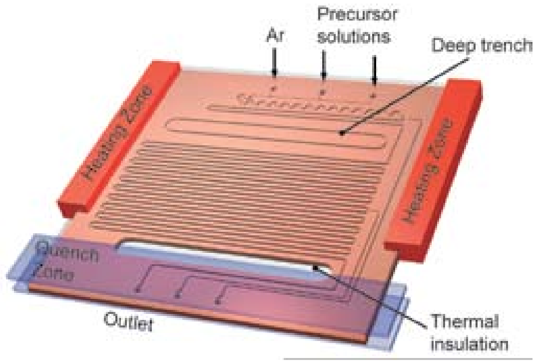

Figure 1: Diagram of the reactor with heated reaction and cooled outlet regions. A through-etch section ensures that the two regions are thermally isolated.

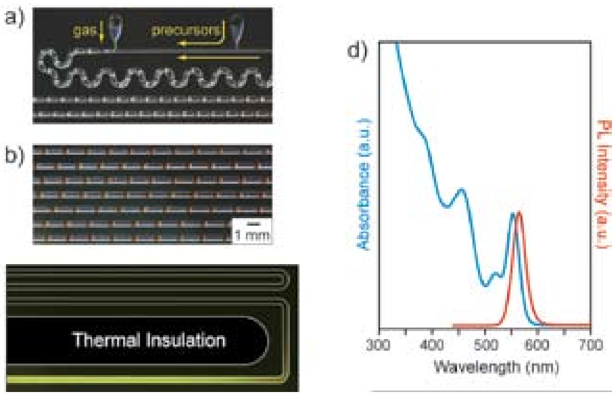

Figure 2: (a) and (b) Images of the heated inlet main channel sections of device during synthesis. Red segments: CdSe QD reaction solution. Dark segments: Ar gas. (c) Time-exposure image of the cooled outlet region under UV irradiation. At reaction temperature (260°C), the QD photoluminescence (PL) is completely quenched, but once the fluid reaches the cooled region (<70°C), yellow PL is observed. (d) Absorbance (blue) and photoluminescence (red) spectra of a typical QD sample prepared in the reactor.

Combinatorial Sensing Arrays of Phthalocyanine-based Field Effect Transistors

M. Bora, T. Heidel, M.A. Baldo, in collaboration with D. Schut (Hewlett-Packard)

Of the millions of molecular species floating in the air or dissolved in water, a substantial fraction can be smelled and uniquely discriminated [1]. Biological systems achieve this functionality with a multitude of non-specific receptors. In this project, we are developing gas sensors based on combinatorial arrays of organic transistors. The combinatorial approach reduces the need to develop specific receptors for each and every molecule of interest. Rather, our sensors are based on exploiting the wide variation in interactions between molecules and metal ions [2], an approach previously employed in colorimetric sensors [3].

We have fabricated gas-sensitive organic transistors each consisting of an approximately 10nm-thick polycrystalline layer of a metallophthalocyanine (MPC) with a gold source and drain contacts. The width and length of the channel for each transistor is 2mm and 50μm, respectively. The current-voltage characteristics of a typical MPC transistor are shown in Figure 1. The charge carrier mobility is typically between 10^{-3} and 10^{-4} cm^2/Vs but the transconductances of various MPC transistors (CoPC, CuPC, ZnPC, and NiPC) are observed to vary when exposed to different gases (acetone and methanol), generating a characteristic response signature for each gas. On interaction with the gas molecules, the energy levels of a given MPC may decrease, disrupting charge transport and possibly forming charge traps in the channel. In some cases, however, the current is observed to increase, possibly due to morphological changes in the channel or doping. Morphological changes in the channel may also lead to drain current instabilities that are typically observed in the first few minutes of operation. Since the sensors can be manufactured simply by inkjet printing on a patterned substrate, these sensors may find application as single-use diagnostic aids.

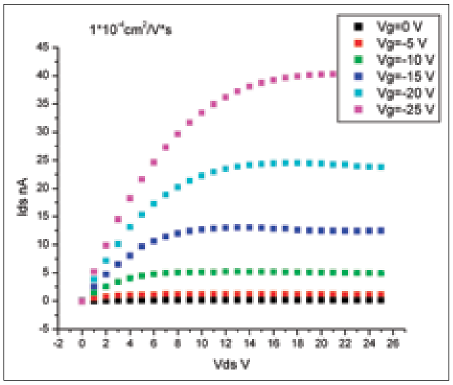

Figure 1: The current-voltage characteristics for a metallophthalocyanine (CoPC) transistor.

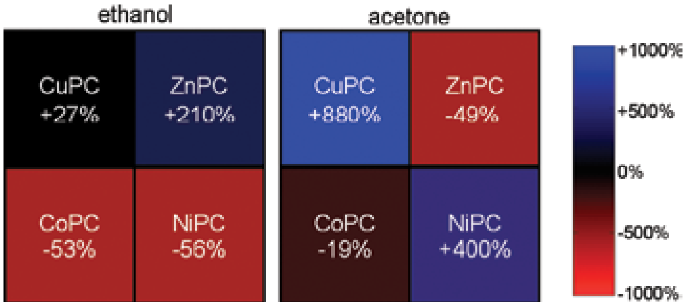

Figure 2: Changes in drain current for phthalocyanine-based organic transistors with V_{GS} = -25V when exposed to saturated vapors of ethanol (left) and acetone (right). The differing patterns are signatures of each gas.

REFERENCES:

[1] Mombaerts, P., "Seven-transmembrane Proteins as Odorant and Chemosensory Receptors," *Science*, vol. 286, pp. 707-711, 1999.

[2] Wang, J., Z.A. Luthey-Schulten, K.S. Suslick, "Is the Olfactory Receptor a Metalloprotein?" *Proceedings of the National Academy of Sciences of the United States of America*, vol. 100, no. 6, pp. 3035-3039, March 2003.

[3] Rakow, N.A., K.S. Suslick, "A Colorimetric Sensor Array for Odor Visualization," *Nature*, vol. 406, no. 6797, pp. 710-713, 2000.

Electrical and Optical Characterization of Photosynthetic Complexes

M. Segal, M.A. Baldo

Sponsorship: DARPA/AFOSR, NSF Nanoscale Interdisciplinary Research Team

Photosynthetic protein complexes employ molecular components positioned with a precision beyond the limits of contemporary fabrication technologies [1] and achieve internal quantum efficiencies approaching 100%. We are optically and electrically characterizing reaction center complexes from R. sphaeroides to evaluate their usefulness in solid-state devices. The complexes are self-assembled into nanofabricated structures in an oriented fashion by selective binding of polyhistidine tags to Ni^{2+}-functionalized gold [2].

We have fabricated a field-effect transistor geometry (Figure 1) using a combination of photolithography, electron beam lithography, and electroplating to achieve source-drain separations comparable to the size of the complex. Complexes form the channel of the device. This geometry may provide insight into the transport that occurs inside the complex. We are also constructing a transparent, two-terminal structure using a poly(dimethylsiloxane) stamp for use in ultrafast optical pump and pump-probe measurements of self-assembled complexes under electrical bias. These measurements should yield the open circuit voltage and fill factor of these biological photovoltaic structures.

Once a test platform has been constructed, the protein complexes can be genetically engineered and the effects on performance and function quantitatively measured. For example, the complexes from R. sphaeroides have been modified to remove the H protein subunit as in Figure 2, allowing close contact to be made to the terminal electron acceptor in the internal electron pathway. This data will allow us to assess the prospects for functional molecular electronic devices based on biological models.

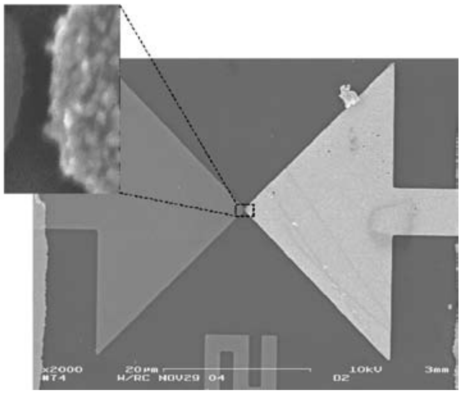

Figure 1: A field-effect transistor geometry test bed for studying protein complex function. The complexes are self-assembled into the channel.

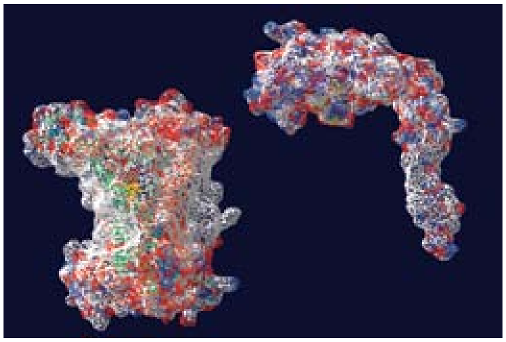

Figure 2: The protein complex from R. sphaeroides can be genetically engineered to remove the H protein subunit (right). Image courtesy of Nikolai Lebedev.

REFERENCES:

[1] Hoff, A.J., J. Deisenhofer, "Photophysics of Photosynthesis: Structure and Spectroscopy of Reaction Centers of Purple Bacteria," Physics Reports, vol. 287, no. 1-2, pp. 1-247, August 1997.

[2] Das, R., P.J. Kiley, M. Segal, J. Norville, A.A. Yu, L. Wang, S.A. Trammell, L.E. Reddick, R. Kumar, F. Stellacci, N. Lebedev, J. Schnur, B.D. Bruce, S. Zhang, M.A. Baldo, "Integration of Photosynthetic Protein Molecular Complexes in Solid-State Electronic Devices," Nano Letters, vol. 4, no. 6, pp. 1079-1083, May 2004.

Integration of Photosynthetic Protein Molecular Complexes with Organic Semiconductors

J. Mapel, M. Singh, M.A. Baldo

Sponsorship: DARPA/AFOSR, NSF Nanoscale Interdisciplinary Research Team

Over two billion years of evolutionary adaptation have optimized the functionality of biological photosynthetic complexes. Plants and photosynthetic bacteria, for example, contain protein molecular complexes that harvest photons with nearly optimum quantum yield and an expected power conversion efficiency exceeding 20%. The molecular circuitry within photosynthetic complexes is organized by a protein scaffold, at a density that cannot be matched by alternate technology. Indeed, if integrated with solid-state electronics, photosynthetic complexes may offer an attractive architecture for future generations of circuitry.

Stabilizing the complexes in an artificial environment is the key barrier to successful device integration [1]. We used novel surfactant peptides [2] to stabalize an oriented, self-assembled monolayer of reaction centers (RCs) found in *R. sphaeroides* (Figure 1). The same process worked with Photosystem I taken from spinach. Subsequently, an organic semiconducting protective coating was deposited as a buffer to prevent damage during fabrication of the top metal contact. Fabricating solid-state photodetectors and photovoltaic devices verified the functionality of the complexes. The internal quantum efficiency of the first generation of devices was estimated to be 12%. Successful integration was conclusively demonstrated by comparisons of the absorption spectrum and photocurrent spectra shown in Figure 2. Further work will harness the full (up to 1.1V) open circuit voltage of complexes, such as Photosystem I, and enhance the optical cross section of these devices.

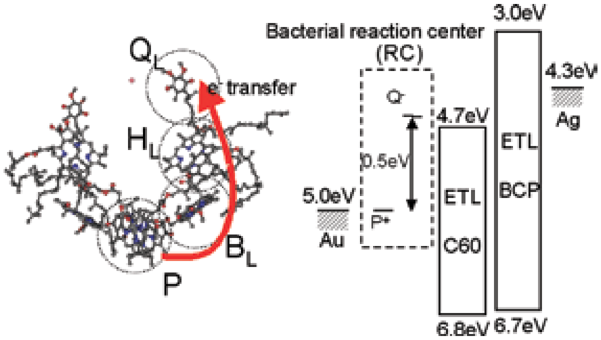

Figure 1: (left) The internal molecular circuitry of a photosynthetic bacterial reaction center with the protein scaffold removed for clarity. The complex is only a few nanometers top-to-bottom. After photoexcitation, an electron is transferred from the special pair, P, to the quinone, Q_L. The process occurs within 200 ps, at nearly 100% quantum efficiency, and results in a 0.5V potential across the complex. (right) Energy level diagram of an RC photovoltaic cell.

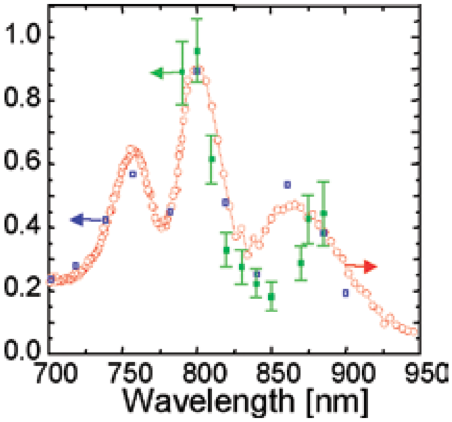

Figure 2: The photocurrent spectrum of solid-state photovoltaic devices employing bacterial reaction centers (RCs). A comparison between the photocurrent spectrum of solid-state (in green) and wet electrochemical cell devices (in blue), and the solution absorption spectrum of the bacterial reaction centers (in red), demonstrates that the observed photocurrent originates in the RCs.

REFERENCES:

[1] Das, R., P.J. Kiley, M. Segal, J. Norville, A.A. Yu, L. Wang, S. Trammell, L.E. Reddick, R. Kumar, S. Zhang, F. Stellacci, N. Lebedev, J. Schnur, B.D. Bruce, M. Baldo, "Integration of Photosynthetic Protein Molecular Complexes in Solid-State Electronic Devices," *Nano Letters*, vol. 4, no. 6, pp. 1079-1083, 2004.

[2] Kiley, P., X. Zhao, M. Vaughn, M.A. Baldo, B.D. Bruce, S. Zhang, "Self-Assembling Peptide Detergents Stabilize Isolated Photosystem I on a Dry Surface for an Extended Time," *PLoS Biology,* accepted, 2005.

Interface Disorder and Charge Injection into Organic Semiconductors

B.N Limketkai, M.A. Baldo

Sponsorship: MARCO MSD

In this project, we examine the effect of structural disorder at the injection interface on the current-voltage (IV) characteristics of organic semiconductors. We find that structural disorder at the injection interface creates energetic disorder, which effectively generates deep interface traps that are observed to dominate the IV characteristics of these materials. For metal electrodes, interfacial energetic disorder is due primarily to variation in the image charge effect on a rough metal surface. Modeling the metal surface as self-affine fractal, we find that the standard deviation in the energy levels of the semiconductor is: $\sigma(z_0) \approx q^2 w/8\pi\varepsilon_r\varepsilon_0 z^2$, where z is the distance from the metal interface, w is the global rms roughness of the metal interface, q is the electron charge and $\varepsilon_r\varepsilon_0$ is the permittivity [1]. Most notably, for equally spaced molecular layers, the $1/z^2$ decay yields the ratio of standard deviations of transport energy levels in the first and second molecular layers, σ_1 and σ_2, to be 4. This result is *independent* of material parameters such as the surface roughness. The current density is determined by the rate of charge hopping from the interfacial layer to less disordered sites in the second molecular layer [2] as shown in Figure 1. Using the Marcus expression for charge hopping between Gaussian distributions gives a master equation: $J=J_0(V+\Delta V)^m/V_0^m$, where ΔV is the cathode doping-dependent voltage shift, and J_0 and V_0 are constants [1]. The power law slope $m=1+\sigma_1^2/(\sigma_2^2+2\lambda kT)$, where λ is the reorganization energy of the molecule. At low temperatures, the decay of energetic disorder gives a constant $m=1+\sigma_1^2/\sigma_2^2 \approx 17$.[1] In order to demonstrate the universality of the model, the IV characteristics of a wide variety of electron injection contacts are shown in Figure 2. The power law slope is constant at $m = (20\pm1)$ at 10K, independent of the choice of cathode or organic material.

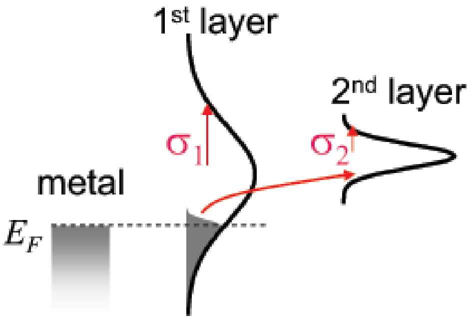

Figure 1: Charge injection when dominated by interface traps.

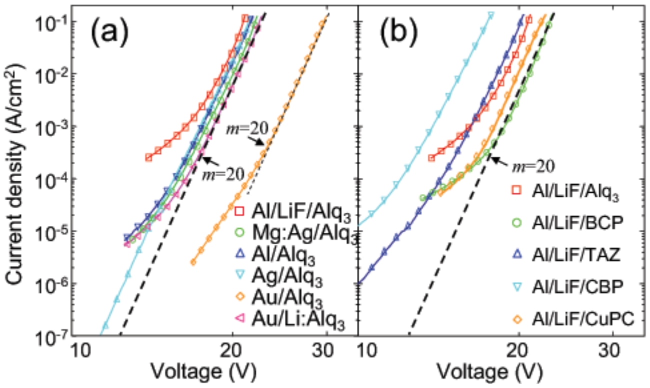

Figure 2: The IV characteristics at T = 10K for (a) Alq_3 interfaces, and (b), a comparison of Al/LiF contacts to Alq_3, BCP, TAZ, CBP, and CuPC. All cathodes exhibit similar power law behavior, i.e. $J \sim V^m$, where m = (20±1), demonstrating that electron injection at these interfaces is not controlled by an energy barrier between the metal and organic semiconductor.

REFERENCES:

[1] Limketkai, B.N., M.A. Baldo, “Charge injection into cathode-doped amorphous organic semiconductors,” *Physical Review B: Condensed Matter and Materials Physics,* vol. 71, no. 8, article 085207, February 2005.

[2] Baldo, M.A., S.R. Forrest, “Interface-limited injection in amorphous organic semiconductors,” *Physical Review B: Condensed Matter and Materials Physics*, vol. 64, no. 8, article 085201, August 2001.

Nanopattern-assisted Growth of Organic Materials for Device Applications

D. Mascaro, R. Tabone, V. Bulovic

Sponsorship: NSF, MARCO MSD

The challenge of generating crystals of organic materials has been pursued by many research groups who aim to develop materials sets for active electronic and optoelectronic devices, including field-effect transistors, photodetectors and optical modulators. We developed a method for in-plane growth of millimeter-scale crystalline organic needles from initially amorphous thin films of the molecular organic semiconductor tris(8 hydroxyquinoline)aluminum (Alq_3). The needles form when the vacuum-deposited amorphous films are exposed to chloroform vapor at room temperature and pressure, and can be as large as several microns thick, several microns wide, and one centimeter long (limited in length by the substrate dimensions). As such, the Alq_3 needles are more than 100 times longer than any previously reported organic crystals formed in the plane of the substrate. Moreover, the Alq_3 needles are spatially separated from one another and oriented with their long axes parallel to lithographically pre-defined periodic submicron grooves in the substrate surface.

The distinct facets (Figure 1b) and diamond-shaped cross sections (Figure 1c) of the fabricated Alq3 needles are indicative of crystallinity. The optical smoothness of the needle facets is evidenced in fluorescence micrographs that show waveguiding of the Alq3 fluorescence with outcoupling occurring at the needle edges and defects (Figure 1a). Polarized fluorescence measurements show a change in luminescence intensity with polarization angle, with a maximum at ~15 degrees from the long axis of the needle (Figure 2a). Fluorescence spectra of the crystal needles, obtained via confocal microscopy, peak at energy of 2.36 eV (peak wavelength of 525 nm) in agreement with the previously reported spectrum of polycrystalline Alq_3 (Figure 2b).

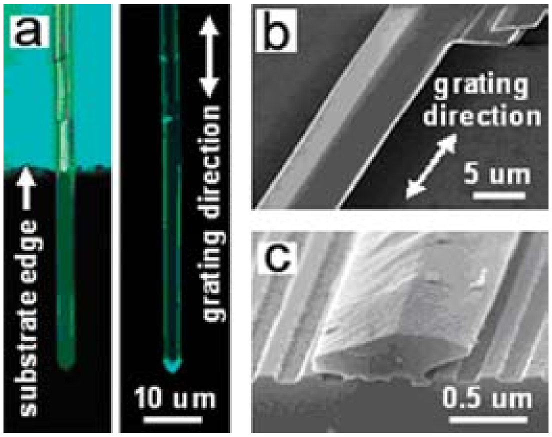

Figure 1: Alq_3 crystalline needles formed by exposure of amorphous Alq_3 thin films to chloroform vapor at room temperature. (a) Optical micrograph (left) and fluorescence micrograph (right, 365 nm excitation wavelength) of an Alq_3 needle that extends ~35 µm beyond the substrate edge. (b) Scanning electron micrograph (SEM) showing the distinct facets of an Alq_3 needle. (c) SEM showing the typical diamond-shaped cross section of an Alq_3 needle.

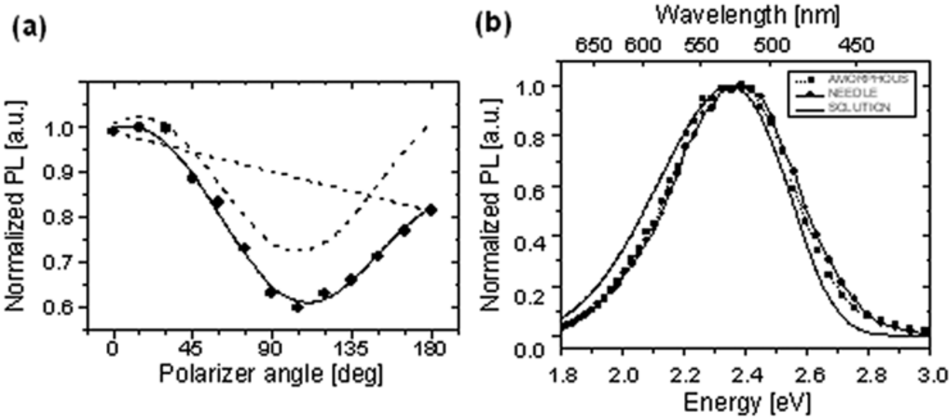

Figure 2: Fluorescence of Alq_3 needles. (a) Plot of the normalized photoluminescence (PL) intensity (365 nm excitation wavelength) as a function of polarizer angle, where 0 degrees corresponds to the polarizer aligned with the long axis of the needle. The decrease in fluorescence intensity from 0 to 180 degrees is due to gradual photooxidation of the Alq_3 during the measurement as indicated by the straight dashed line. The sinusoidal response of PL with polarizer angle and the composite of the PL response and the gradual oxidation are plotted in dashed and solid lines, respectively. (b) Fluorescence spectra (365 nm excitation wavelength) of an as-deposited Alq_3 thin film and an Alq_3 crystal needle, obtained via confocal microscopy. The solution fluorescence spectrum (408 nm excitation wavelength) of Alq_3 in chloroform is also plotted.

Fabrication of Polysilicon Electrode Pattern for Growing Aligned, Single-Wall Carbon Nanotubes

H. Son, Y. Hori, S.G. Chou, D. Nezich, G.G. Samsonidze, G. Dresselhaus, M.S. Dresselhaus

Sponsorship: NSF, Intel

Single-wall carbon nanotubes (SWNTs) are envisioned for a new form of electronic, optical, and chemical sensing devices. Two of the greatest challenges in integrating SWNTs with standard silicon technology are positioning them and aligning them. In this work, we present a new way of aligning and positioning the SWNTs in a regular array. The SWNTs are grown across two poly-Si electrodes, which serve both as electrical contacts and as elevated structures for suspending the SWNTs. The poly-Si electrodes are fabricated using standard silicon technology [Figure 1(a)]. First, a 1-μm-thick poly-Si film is grown by chemical vapor deposition (CVD) on top of a thermally-grown 1-μm-thick SiO$_2$ film on a silicon substrate. Then, photolithography and a reactive-ion etching are used to pattern the poly-Si film and the oxide film. The electrodes contain two regions: the narrow trench region (1~4μm wide) and the wide trench region (10μm wide), as Figure 1(b) shows. During the SWNT growth, a high electric field on the order of 10^6V/m can be selectively applied across the narrow trenches only. A high electric field is known to enhance the growth rate of SWNTs and to align them [1,2]. Moreover, controlling the maximum length of the SWNTs can guarantee that no suspended SWNTs grow across the wide trench [Figure 1(c)]. The SWNTs are grown directly on the sample by a methane-CVD process. Samples were prepared both with and without applied electric fields between the electrodes, as Figures 1(d) and 1(e) show. Using the presented electrode structure along with the electric field during the SWNT growth produces well-aligned SWNTs in a regular array.

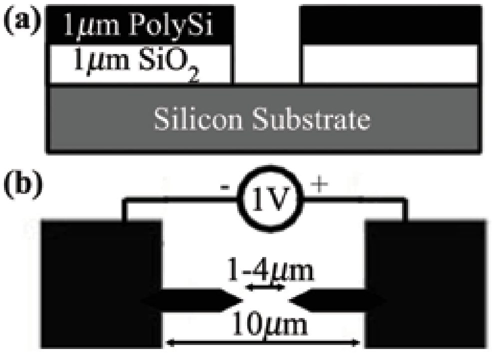

Figure 1: The schematic of (a) the side view and (b) the top view of the electrode structure.

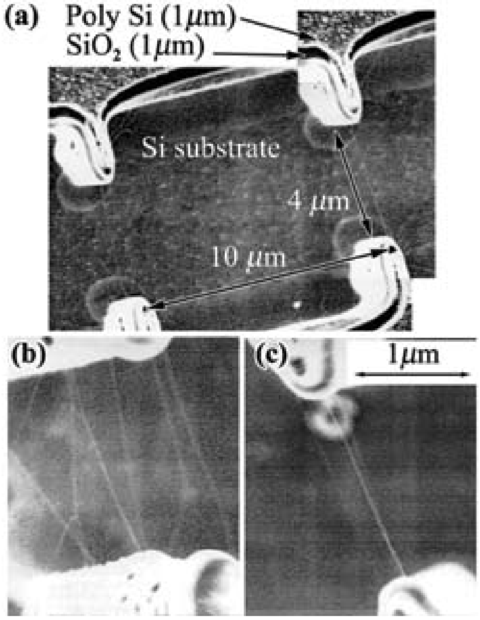

Figure 2: (a) and (c) Suspended SWNTs grown with an applied electric field. (b) Suspended SWNTs grown without an applied electric field. The magnification is the same for (b) and (c).

REFERENCES:

[1] Ono, T., H. Miyashita, and M. Esashi, "Electric-field-enhanced Growth of Carbon Nanotubes for Scanning Probe Microscopy," *Nanotechnology*, vol. 13, no. 1, pp. 62-64, February 2002.

[2] Zhang, Y., A. Chang, J. Cao, Q. Wang, W. Kim, Y. Li, N. Morris, E. Yenilmez, J. Kong, and H. Dai, "Electric-field-directed Growth of Aligned Single-Walled Carbon Nanotubes," *Applied Physics Letters*, vol. 79, no. 19, pp. 3155-3157, November 2001.

Carbon Nanotube Machine Elements: Components of Small-scale, Compliant Mechanisms and Positioning Equipment

K. Lin, M. Culpepper

Sponsorship: Rockwell International Career Development Chair, NSF Nanomanufacturing Program

We are investigating the design and fabrication challenges that must be overcome to enable the use of carbon nanotubes (CNTs) as flexure hinges in small-scale compliant mechanisms (CMs) and machines. In CMs, motion is guided by the compliance of some or all of the mechanism's members. The CMs are not beam-like springs; rather, they are systems of compliant-rigid elements that combine to produce a mechanism capable of large and controlled motions in multiple degrees-of-freedom (DOF). These CMs do not require sliding, rolling, or other types of contact bearings (e.g., pin-in-hole prismatic joints) often found in rigid mechanisms. Therefore, CMs provide three unique advantages: 1) eliminate position inaccuracy due to friction; 2) eliminate joint wear and its affect on longevity; and 3) eliminate joint clearance that affects the mechanism's accuracy. The CNTs are attractive as flexure hinges, due to their large rotational capabilities and their high strain-strength characteristics in a kinked mode. Figure 1 shows the simulated shape of a kinked CNT [1]. The CNTs' deformation characteristics would enable CNT-based CMs to experience large deformations and, therefore, exhibit a range of motion that is much larger than that which could be obtained by traditional materials (e.g., silicon). CNT flexure hinges may then be combined with structural elements and nano-scale sensors, actuators, and electronics to form the core of next generation nanomechanical systems such as nano-scale positioners [2] and nano-scale end effectors [3, 4]. Figure 2 shows a concept for a single DOF device that is being examined. In Figure 2, CNTs form the rotational joints between the links of a mechanism. In the nascent stages of this work, we are generating a design theory, fabrication processes and testing processes required to develop small-scale, CNT-based machines for precision positioning.

Figure 1: Simulated bending of single wall CNT [1].

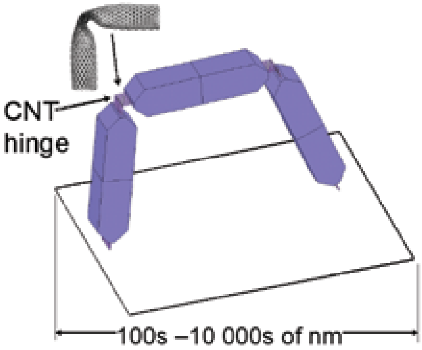

Figure 2: A CNT-based, four bar mechanism.

REFERENCES:

[1] Iijima, S., C. Brabec, A. Maiti, J. Bernholc, "Structural Flexibility of Carbon Nanotubes," *Journal of Chemical Physics*, vol. 104, no. 5, pp. 2089-2092, 1996.

[2] Chen, S., M.L. Culpepper, "Compliant Mechanisms for Micro-scale Spatial Manipulators: Applications in Nanomanipulation," *Nineteenth Annual American Society for Precision Engineering Meeting*, Orlando, FL, pp. 293-296, October 2004.

[3] Akita, S., Y. Nakayama, "Manipulation of Nanomaterial by Carbon Nanotube Nanotweezers in Scanning Probe Microscope," *Japaneese Journal of Applied Physics*, vol. 41, part 1, no.6B, pp. 4242-4245, Jun. 2002.

[4] Lee, J., S. Kim, "Manufacture of a Nanotweezer Using a Length-Controlled CNT Arm," *Sensors and Actuators A: Physical*, vol. 120, no. 1, pp. 193-198, April 2005.

Nanoelectromechanical Memories and Switches

K. Milaninia, M.A. Baldo

Sponsorship: MARCO MSD, ISN

The ability to change shape is a compelling attraction of molecular semiconductors. Compared to rigid inorganic materials, molecules are soft and malleable, and their conformational changes are essential to the functionality of biological systems. Applications of nano-electromechanical (NEM) molecular devices include memories and transistors. Information can be stored in the conformation of molecules, potentially leading to very high density memories, and molecular transistors that change shape under bias could exhibit subthreshold slopes of << 60 mV/decade [1]. Indeed, as an example of the potential of NEMs, voltage-gated ion channels possess subthreshold slopes of approximately 15 mV/decade [2].

Although many materials are available for NEM applications, carbon nanotubes exhibit low resistance and good mechanical properties. In this project, we are constructing a NEM testbed. The proposed design for our relay is shown in Figure 1. Nanotubes are directly grown at the bottom of a electron-beam defined trench etched in Si. This offers better control over the nanotubes and removes the need for additional steps that are required for the removal of surfactants and organics from the surface of the nanotubes. Because the nanotubes are vertically oriented, we are able to take advantage of the smallest size feature of the carbon nanotube: its diameter. This allows us to create dense arrays of relays for applications such as memory or logic devices. The vertical orientation allows NEM structures with very large aspect ratios. Theoretical results [3] have shown that increasing the aspect ratio of a carbon nanotube reduces the voltage needed to pull in the nanotube, thereby reducing the power requirement. Furthermore, because of the ability to easily functionalize the surface of nanotubes, we can functionalize the tube with charge to lower the pull-in voltage even further.

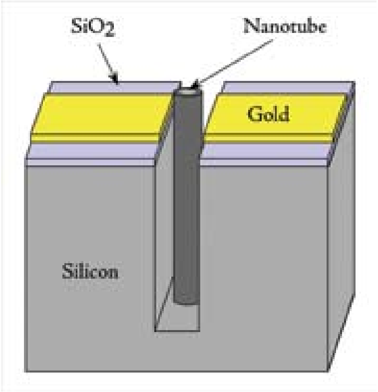

Figure 1: Schematic of the proposed device.

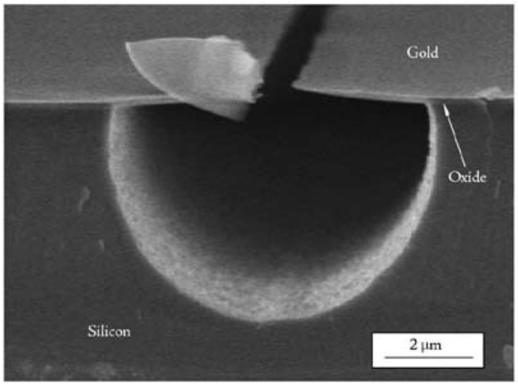

Figure 2: Actual device without nanotube.

REFERENCES:

[1] Ghosh, A.W., T. Rakshit, S. Datta, "Gating of a Molecular Transistor: Electrostatic and Conformational," *Nano Letters*, vol. 4, no. 4, pp. 565-568, 2004.

[2] Hodgkin, A.L., A.F. Huxley, "Currents Carried by Sodium, Potassium Ions Through the Membrane of the Giant Squid Axon of Logilo.," *Journal of Physiology*, vol. 116, no. 4, pp. 449-472, April 1952.

[3] Dequesnes, M., S.V. Rotkin, N.R. Aluru, "Calculation of Pull-in Voltages for Carbon-Nanotube-Based Nanoelectromechanical Switches," *Nanotechnology*, vol. 13, no. 1, pp. 120-131, February 2002.

Carbon Nanotube Rings for Interconnect and Device Applications

B. Wunsch, T.M. Wu, F. Stellacci, R. Reif

Sponsorship: NSF, MARCO IFC

Carbon nanotube rings have potential applications for both CMOS interconnects and devices. As copper interconnect dimensions shrink, the copper bulk resistivity is expected to increase due to surface scattering effects. An alternative to standard copper interconnects is to use carbon nanotubes, which have demonstrated ballistic transport properties and high achievable current densities.

We are currently investigating a method by which pre-grown carbon nanotubes are assembled onto a surface to form an interconnect structure. One of the key steps to achieving carbon nanotube interconnects through this self-assembly method is a suitable purification procedure. The fact that carbon nanotube rings demonstrate magnetic behavior provides us with a relatively simple and undamaging way to separate the magnetic, nanotube-containing fraction of a particular sample from the nonmagnetic, undesirable material. In addition, we are investigating the possibility of using these carbon nanotube rings as inductors in CMOS circuits. We have observed carbon nanotube rings with diameters in the range of hundreds of nanometers. Because current state-of-the-art CMOS metal inductors are generally tens to hundreds of microns in size, if these nanotube rings are suitable for inductor applications, we can achieve a dramatic improvement in device density.

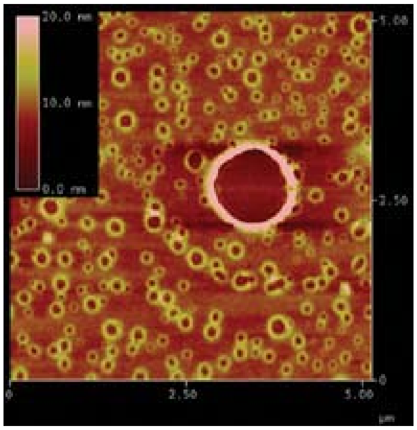

Figure 1: Tapping-mode atomic force microscope height image of single-walled carbon nanotube rings.

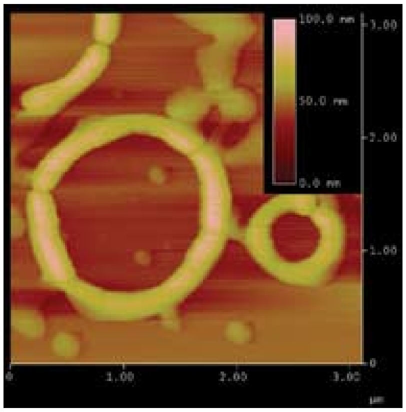

Figure 2: Tapping-mode atomic force microscope height image of multi-walled carbon nanotube rings.

Measuring Thermal and Thermoelectric Properties of Single Nanowires

C. Dames, C.T. Harris, G. Chen, in collaboration with M.S. Dresselhaus (MIT), Z.F. Ren (Boston College), J.P. Fleurial (JPL)

Sponsorship: Department Of Energy

Knowledge of nanowire thermal and thermoelectric properties will be important for the thermal management of nanowire devices (optoelectronic, sensing, and computing) and essential for the design of nanowire thermoelectric materials. For nanowire diameters smaller than the bulk mean free path of heat carriers, theory predicts that the thermal conductivity of nanowires will be reduced when compared to similar bulk materials [1, 2]. To experimentally verify these predictions, we are exploring several systems to measure the physical properties of single nanowires.

Our current work includes a basic platform to measure the thermal conductivity and specific heat of electrically conducting nanowires, such as the microfabricated metal lines shown below in Figure 1. Joule heating of a suspended nanowire with thermally clamped ends results in a temperature rise of the nanowire due to its finite thermal resistance. This temperature rise can be measured by resistance thermometry (again using the nanowire) and used to calculate its thermal conductivity and specific heat. This technique is being adapted for an in-situ transmission electron microscopy (TEM) measurement. If successful, this method will permit high-throughput physical property measurements of many nanowires of various geometries and morphologies, and allow correlations with their atomic structure as determined by TEM.

Microfabricated metal lines can also be employed to measure electrically insulating nanowires. Using electron beam lithography, a metal heater line is fabricated such that a target nanowire crosses the center of the line. With the nanowire and heater thermally anchored, the nanowire removes a fraction of heat from the heater line. This reduces the heater's temperature rise, and thus makes it possible to calculate the thermal resistance of the nanowire.

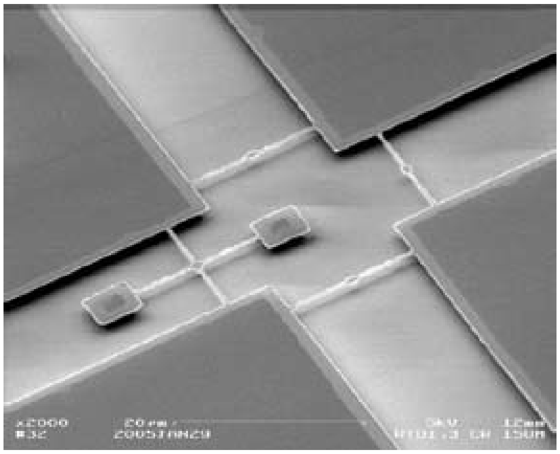

Figure 1: Microfabricated metal heater lines suspended 1.0 µm above the substrate, for thermal property measurements.

REFERENCES:

[1] Dames, C., G. Chen, “Theoretical Phonon Thermal Conductivity of Si/Ge Superlattice Nanowires,” *Journal of Applied Physics*, vol. 95, no. 2, pp. 682-693, January 2004.

[2] Chen, G., Nanoscale Energy Transport and Conversion, New York: Oxford University Press, 2005.

Growth of High-quality Single-walled Carbon Nanotube Films on Flat and Microstructured Silicon Substrates

A.J. Hart, A.H. Slocum

Sponsorship: MIT Deshpande Center, Fannie and John Hertz Foundation

With the outstanding mechanical, electrical, thermal, and optical properties of carbon nanotubes (CNTs) now widely established [1,2], there is an emerging need for materials and methods that integrate carbon nanotubes as thin-films in standard microelectronic and micromechanical fabrication processes. We have developed a simple, versatile, and repeatable method for growing high-quality CNTs on silicon substrates by atmospheric pressure thermal chemical vapor deposition (CVD), from an $Mo/Fe/Al_2O_3$ catalyst film that is deposited entirely by electron beam evaporation. High-density single-walled CNT films having a Raman G/D ratio of at least 20 are grown over a temperature range of 750-900 °C. Within a broad parametric study, the highest yield is obtained from a mixture of approximately 20%/80% H_2/CH_4 at 825 °C. We also observe a novel growth behavior on long samples in pure CH_4, where the quality and density of the CNTs change distinctly as the chemistry of the gas evolves with the flow of the boundary layer along the sample. We demonstrate that simply placing another piece of silicon wafer as a “cap” over the catalyst-coated sample further increases the yield and quality of CNTs and enables uniform growth over large substrate areas, where the gas flow is limited by diffusion between the cap and the sample.

Using the same catalyst deposition and CVD processes, we also grow uniform CNT films on a variety of silicon microstructures, including vertical sidewalls fabricated by reactive ion etching and angled surfaces fabricated by anisotropic wet etching. Comparative experiments suggest that molybdenum (Mo) is critical for high-yield SWNT growth from Fe in H_2/CH_4, yet leads to poor-quality multi-walled CNTs (MWNTs) in H_2/C_2H_4. An exceptional yield of vertically-aligned MWNTs is obtained using Fe/Al_2O_3 in H_2/C_2H_4. These results emphasize the synergy between the catalyst and gas activity in determining the morphology, yield, and quality of CNTs grown by CVD, and enable direct growth of CNTs in microsystems for a variety of applications.

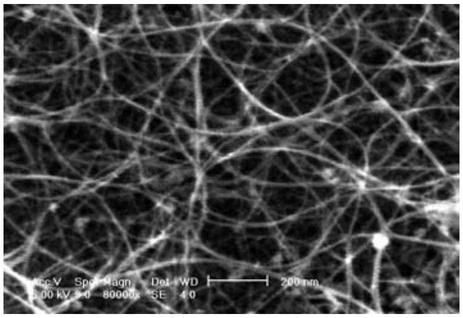

Figure 1: A CNT film grown using 80%/20% CH_4/H_2 at 825 °C, from $Mo/Fe/Al_2O_3$ catalyst deposited on polished (100) Si.

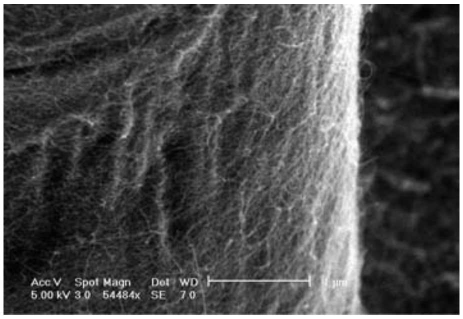

Figure 2: A CNT film grown on vertical sidewall of silicon post etched in STS-DRIE.

REFERENCES:

[1] Baughman, R.H., A.A. Zakhidov, W.A. de Heer, “Carbon Nanotubes - The Route Toward Applications,” *Science*, vol. 297, pp. 787-792, 2002.

[2] Endo, M., T. Hayashi, Y.A. Kim, M. Terrones, M.S. Dresselhaus, “Applications of Carbon Nanotubes in the Twenty-first Century,” *Philosophical Transactions of the Royal Society,* vol. 362, pp. 2223-2238, 2004.

Carbon Nanotube Modification and Characterization

T.M. Wu, F. Stellacci, R. Reif

Sponsorship: MARCO IFC

We are currently investigating the modification and characterization of carbon nanotubes for CMOS interconnect applications. Due to surface scattering effects, the amount of copper increases dramatically as interconnect dimensions shrink the bulk resistivity of the state-of-the-art material. As a result, efforts are being made to find alternative interconnect solutions. One promising candidate is carbon nanotubes because of to their potential ballistic transport properties and resistance to electromigration. However, many obstacles must be overcome for carbon nanotube interconnects to become viable. One of these obstacles is the formation of the actual interconnect structure.

There are two methods to form a carbon nanotube structure on a surface (Figure 1). The first method is to directly grow the nanotubes on the surface in the desired pattern. The second method is to assemble already-grown nanotubes into a pattern on the surface. Our work focuses on developing a process for the second method, self-assembly of nanotubes onto a patterned surface (Figure 2). The proposed process consists of four steps: purification, modification, patterning, and self-assembly. In the first step, we purify the raw as-grown nanotubes by removing amorphous carbon and metal catalyst particles. Next, we modify the purified nanotubes with a chemical handle. Thirdly, we use a complementary chemical handle to write a pattern on the surface. Finally, the nanotubes are assembled onto the surface, driven by the interaction between the chemical handles. We are currently developing a suitable nanotube purification technique and testing different chemical reactions for the nanotube modification and handle-surface interactions.

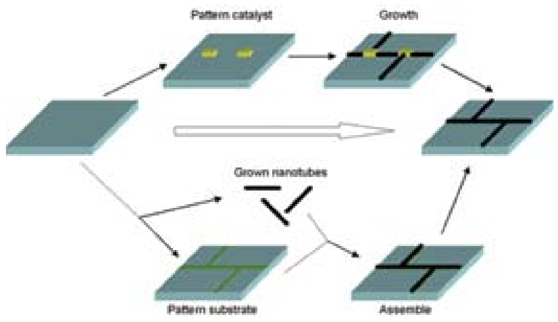

Figure 1: Two routes to carbon nanotube interconnects: direct growth (top) and directed assembly (bottom).

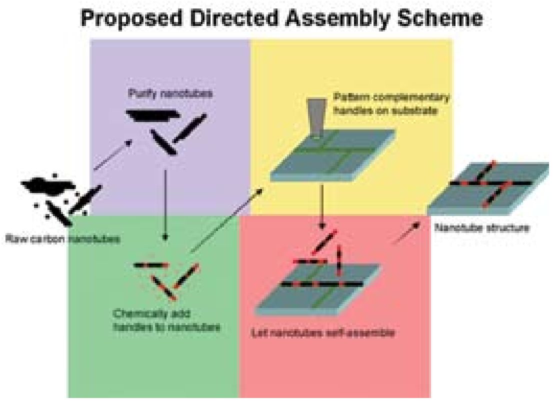

Figure 2: Our proposed four-step assembly scheme.

High-concentration Dispersion of Single-wall Carbon Nanotubes

Y. Sabba, E.L. Thomas

Sponsorship: Cambridge-MIT Institute

We report a novel method to exfoliate and disperse single-wall carbon nanotubes (SWNTs) into organic and aqueous solutions. The method is based on treatment of SWNTs with a solution of hydroxylamine hydrochloric acid salt [$(NH_2OH)(HCl)$] and does not require truncation of the tubes or surface absorption of organic molecules. The solution-dispersed tubes can easily be incorporated into an organic matrix in order to obtain a nanocomposite. We illustrate the method by forming PMMA-SWNT and PS-SWNT nanocomposites. One percent of the SWNT-PMMA nanocomposites, having a draw ratio of ~6, showed a dramatic six times increase in the strain to fracture, compared to fibers of similar draw ratio made from pure PMMA [1].

REFERENCES:

[1] Sabba, Y., E.L. Thomas, “High-Concentration Dispersion of Single-Wall Carbon Nanotubes,” *Macromolecules*, vol. 37, no. 13, pp. 4815-4820, 2004.

Catalyst Engineering for Controlled Growth of Carbon Nanotubes

G.D. Nessim, R. Krishnan, C.V. Thompson

Sponsorship: MARCO IFC

A major challenge in carbon nanotube (CNT) growth is the ability to control the density, type, and position of the nanotubes. One possible approach to obtain CNTs with the desired properties is to engineer the catalyst. We are developing various techniques for templated assembly of ordered arrays of metallic nanodot catalysts. In one technique, perfectly ordered porous alumina is used to create nanodots at the bases of the pores, and nanotubes are grown in a porous alumina scaffold. This process allows production of large ordered arrays of dots and tubes in a scaffold that prevents tube agglomeration and provides a platform for testing of tubes in devices. With this and other techniques, we are prepared to investigate the variations of the properties of the dots themselves, as well as correlate them with corresponding variations in tube properties. We have developed a versatile system for thermal chemical vapor deposition (CVD), and we are investigating growth on patterned and unpatterned catalysts. Catalysts are characterized using X-ray analysis and electron microscopy techniques, and nanotubes are characterized using electron microscopy and Raman spectroscopy. We are also investigating the thermal chemical pretreatment of the catalysts, both with and without nanotube growth.

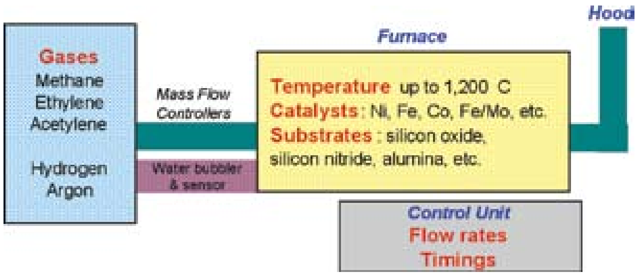

Figure 1: Thermal CVD apparatus for study of carbon nanotube growth with engineered catalysts.

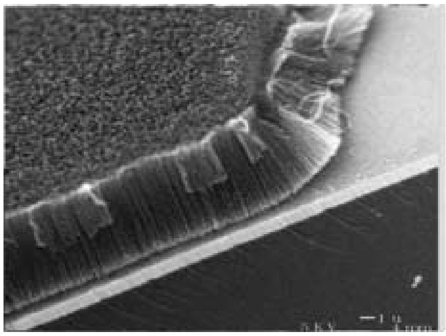

Figure 2: CNT "carpet," grown with thermal CVD. Substrate: Si/SiO_2. Catalyst: Al_2O_3/Fe (100 nm/1 nm). CNT growth at 750°C for 15 minutes. Gases: Ar/H_2 600/400 sccm (through water bubbler). [1]

REFERENCES:

[1] Hata, K., D.N. Futaba, K. Mizuno, T. Namai, M. Yumura, S. Iijima, "Water-Assisted Highly Efficient Synthesis of Impurity-free Single-walled Carbon Nanotubes," *Science*, vol. 306, no. 5700, pp. 1362-1364, November 2004.

Multiple Transistor Devices and Functional Building Blocks on a Single Carbon Nanotube

D.A. Nezich, J. Kong

Sponsorship: EECS

Single-walled carbon nanotubes are promising for future high performance electronics owing to their unique properties, including ballistic transport and compatibility with high-*k* dielectrics. High performance p-type and n-type nanotube field effect transistors (FETs) have been demonstrated [1,2]. So far, most of these studies are based on one transistor per nanotube. We plan to take this research a step further by building multiple devices on one single tube, then eventually building a functional block with complementary tube FET devices. With all the devices made from the same nanotube, we will systematically compare their performance dependence on gate dimensions, contact area, and other parameters. Device characteristics based on nanotube size and chirality will also be evaluated.

REFERENCES:

[1] Javey, A., J. Guo, Q. Wang, M. Lundstrom, H. Dai, “Ballistic Carbon Nanotube Field Effect Transistors,” *Nature*, vol. 424, no. 6949, pp. 654-657, August 2003.

[2] Javey, A. *et al.*, “High Performance N-type Carbon Nanotube Field Effect Transistors with Chemically Doped Contact,” *Nano Letters*, vol. 5, no. 2, pp. 345-348, February 2005.

Investigation of the Synthesis of Carbon Nanotubes

A.R. Cecco, J. Kong

Sponsorship: MARCO IFC

The unique electrical and structural properties of single-walled nanotubes (SWNT) make them very good alternative candidates for interconnect applications. In this project, we will carry out systematic studies on nanotube chemical vapor deposition (CVD) synthesis, with the goal of using nanotube CVDs as interconnects for integrated circuits in the future. Due to the large kinetic inductance in nanotubes, bundles of densely packed SWNTs are more suitable for this application instead of individual SWNTs [1]. However, successfully synthesizing bundles of SWNTs of uniform sizes, as well as controlling their location and orientation, is currently a challenge. The recent result of growing well-aligned SWNTs with H_2O as a weak oxidizer seems very promising [2]. We plan to investigate the H_2O-assisted synthesis of SWNT bundles, first in the vertical geometry, then in the planar geometry on the surface. In addition, we will study the synthesis of individual nanoparticles to understand the growth mechanism of nanotube synthesis.

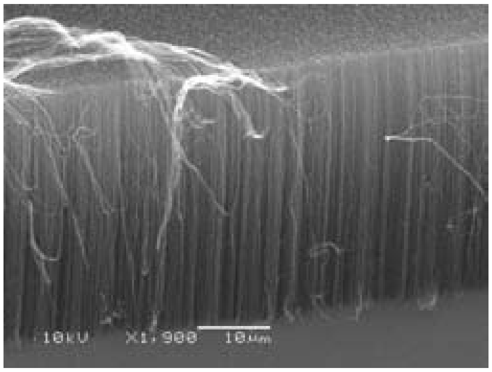

Figure 1: Scanning electron microscope image of vertically aligned nanotubes by H_2O-assisted CVD synthesis.

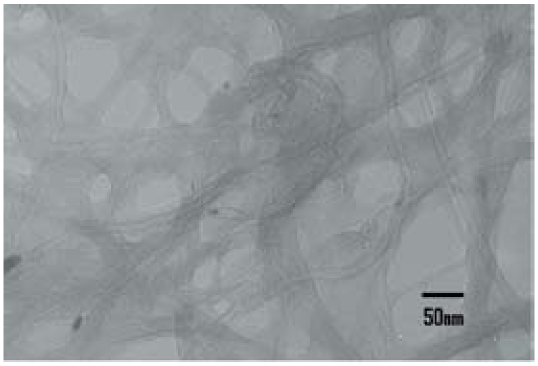

Figure 2: Transmission electron microscope image indicating that these nanotubes are mainly SWNTs; however, there is a significant amount of amorphous carbon present in the sample at the current stage.

REFERENCES:

[1] Naeemi, A., R. Sarvari, and J.D. Meindl, “Performance Comparison between Carbon Nanotube and Copper Interconnects for Gigascale Integration,” *IEEE Electron Device Letters,* vol. 26, no. 2, pp. 84-86, February 2005.

[2] Hata, K. *et al.*, “Water-Assisted Highly Efficient Synthesis of Impurity-free Single-walled Carbon Nanotubes,” *Science,* vol. 306, no. 5700, pp. 1362-1364, November 2004.

Carbon Nanotube Assembly by Nanopelleting

S.D. Gouda, S.-G. Kim

Sponsorship: Intelligent Microsystems Center

We have developed a manufacturing process termed nanopelleting [1,2], which enables large-scale handling and long-range order assembly of individual carbon nanotubes (CNTs). This technique includes vertically growing single-strand CNTs, embedding a CNT into a polymeric pellet, separating the pellet, and transplanting a CNT. CNTs are grown vertically, both individually and in bunches, on the patterned catalytic metal using a Plasma Enhanced Chemical Vapor Deposition (PECVD) machine built by us at MIT (Figure 1). The machine's key feature is the control of the substrate temperature during the growth process. Three thermocouples are connected at the bottom of the ceramic heater to measure the temperature, which is controlled by the heater controller. Plasma is formed between an anode and cathode by applying a DC voltage, which then decomposes acetylene into carbon that deposits below the Ni catalyst and leads to the formation of carbon nanotubes. The process sequence to make pellets containing single strand CNTs is shown in Figure 2. The steps involved in pellet-making process include: (1) coating the silicon wafer with polymethyl methacrylate (PMMA); (2) exposing the photo resists using Raith 150 to obtain the desired patterns (by varying the aperture size, dose, electric field, and developing photo resist); (3) depositing Ti/Ni (25nm) then lifting-off the resist to obtain Ni catalyst nanodots; (4) growing single-stranded CNTs in the PECVD machine with optimized process conditions; (5) spin-coating SU-8 to form a thickness of 25μm on the isolated CNTs; and (6) exposing this SU-8 layer to UV light using an appropriate mask, which forms the nanopellets. The nanopellets are released from the silicon substrate by manually breaking them with a spark needle. We are also developing an in-plane Atomic Force Microscope (AFM) probe with CNT tips assembled mechanically to aid in this process.

Figure 1: PECVD Machine for growing CNTs at MIT

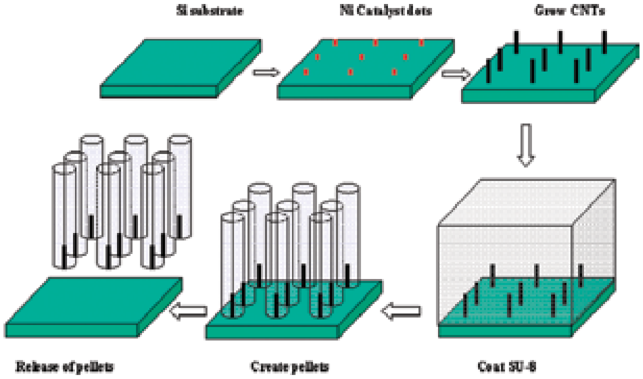

Figure 2: Additive process for nanopellets (single stranded CNT)

REFERENCES:

[1] El-Aguizy, T., S.-G. Kim, "Large-Scale Assembly of Carbon Nanotubes," *ASME Conference on Integrated Nanosystems: Design, Synthesis & Applications*, Pasadena, CA, September 2004.

[2] El-Aguizy, T., J.-H. Jeong, Y.B. Jeon, W.Z. Li, Z.F. Ren, S.-G. Kim, "Transplanting Carbon Nanotubes," *Applied Physics Letters*, vol. 85, no. 24, pp. 5995-5997, December 2004.

Combined Electron Transport with Resonant Raman Spectroscopy Characterization of Carbon Nanotubes

H. Farhat, J. Kong

Sponsorship: CMSE

We plan to study the electron transport in single-walled carbon nanotubes using the Raman spectroscopy technique as a complementary tool to characterize the nanotubes. The work will be carried out in two parts. First, we will perform electrical measurements, so the nanotube type can be identified as semiconducting or metallic. The lineshape of G-band mode with the nanotube type then can be correlated by taking the Raman spectra. The chirality of a nanotube will be identified with Raman spectroscopy and this identification will provide more information toward understanding the electron transport characteristic of the nanotube. Secondly, Raman spectra will be taken while running an electrical current through a nanotube. Stokes and anti-Stokes spectra from Raman will be compared to derive information on the electron-phonon scattering in the nanotubes, which will be important for nanotube interconnect applications.

Nanomagnets and Magnetic Random Access Memories

F.J. Castaño, W. Jung, D. Morecroft, H. Smith, C.A. Ross

Sponsorship: Cambridge-MIT Institute, NSF, Outgoing Marie Curie Fellowship

We are using a variety of lithography techniques (electron-beam lithography, interference lithography, zone-plate-array lithography, photo-lithography and X-ray lithography) to fabricate devices based on arrays of pillars, as well as bar-shaped and ring-shaped 'nanomagnets'. These small structures have thicknesses of a few nanometers and lateral dimensions typically smaller than 100 nm. Arrays of these elements are made with spatial periods of 100 nm and above, using evaporation/sputtering and liftoff, or by etching sputtered film. We are exploring the switching mechanisms of these particles, the thermal stability of their magnetization, and interparticle interactions, and we are assessing their suitability for various data-storage schemes. The behavior of individual particles can be measured using magnetic-force microscopy (MFM), while the collective behavior of arrays of particles can be measured using magnetometry. Data comparison shows how the behavior of one magnet is affected by its neighbors, and how much intrinsic variability there is between the particles as a result of microstructural differences. Small particles have near-uniform magnetization states, while larger ones develop more complex structures such as magnetization vortices or domain walls.

These nanomagnets have potential uses in magnetic random-access memories (MRAM), magnetic logic devices and other magneto-electronic applications. Current MRAM devices rely on bar-shaped multilayered nanomagnets, containing two magnetic layers separated by a thin layer of either a non-magnetic metal (Spin-valves) or an isolator (Magnetic tunneling junctions). The resistance of such elements depends on the relative orientation between the magnetization in the read-out (free) and storage (pinned) layers, allowing for a non-volatile bit of data to be stored in each element. As an alternative bit shape, MRAMs based on ring-shaped multilayered magnets have been recently proposed. We have used a multilevel lithography process to fabricate ring devices made from NiFe/Cu/Co pseudo-spin-valves (PSVs) with non-magnetic contact wires (Figure1). The rings display room temperature giant-magnetoresistance with distinct resistance levels, some of which occur at low applied fields. This feature makes PSV ring attractive for magnetoelectronic applications, such as memories or logic devices. We are currently pursuing a deeper understanding of the magnetization reversal in these multilayered rings using micromagnetic simulations and finite-element analysis.

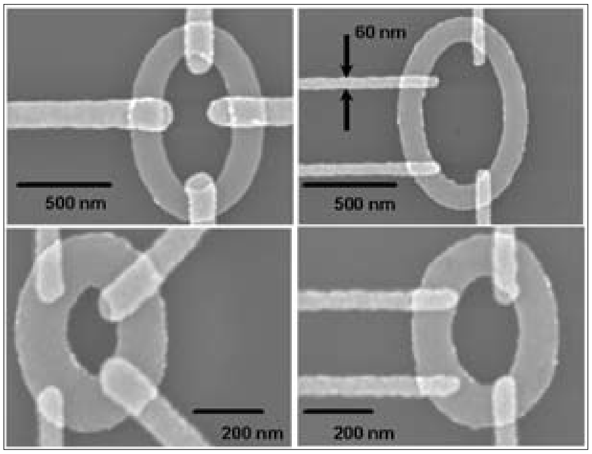

Figure 1: Scanning electron micrographs corresponding to multilayered elliptical-ring devices with different ring dimensions and contact wire configurations. The rings shown are fabricated from a NiFe (6 nm)/ Cu (4 nm)/ Co (4 nm)/ Au (3 nm) multilayer and the contact wires from a Ti (4 nm)/ Au (40 nm) bilayer.

Metal Nanoparticles for Electronic Applications

R. Barsotti, A. Jackson, G. DeVries, P. Djurianovic, F. Stellacci

Sponsorship: NSF, Hewlett-Packard

Ligand-coated AU (gold) nanoparticles have exciting applications in nanoelectronics due to their unique properties derived both from the small size of the metallic core (1-5 nm in diameter) and the ligand molecules that are attached to the nanoparticle by the thiol-gold bond. The ability to alter the composition of these ligands allows for control over the solubility and chemical reactivity of the nanoparticles. Thin films of ligand-coated metal nanoparticles offer the potential for tunable electron-transport properties. Organic ligands coating the nanoparticles act as insulating barriers through which electrons tunnel as they move between metallic cores. The length of the ligands, the degree of conjugation in the ligand shells, and the chemical functionality of the ligands affect the characteristics of that tunneling barrier, allowing a range in the film conductivity from insulating to semi-conducting to metallic. Ligand-coated gold nanoparticles also have shown single-electron charging effects and can be used in the fabrication of a single electron transistor (SET). Bottom-up directed assembly of gold nanoparticles is possible due to the large number of functional groups that can form the head group of a thiolated molecule attached to a gold nanoparticle. This assembly allows for a variety of co-valent or ionic bonding chemistries with molecules patterned on a substrate. An insulating gap is cut in conductive gold wires (fabricated with ebeam lithography) using a focused ion beam. The ends of the gold wires are then functionalized with dip pen nanolithography (DPN), patterning molecules with terminal carboxylic acid or alcohol functionalities. Nanoparticle assembly occurs selectively on the patterned regions. Preliminary results show a 100-times decrease in resistance after nanoparticle assembly. Improved resolution in gap formation and DPN will allow for the assembly of a single nanoparticle in the gap, which will serve as an SET whose electronic properties can be tuned by the choice of surrounding ligands.

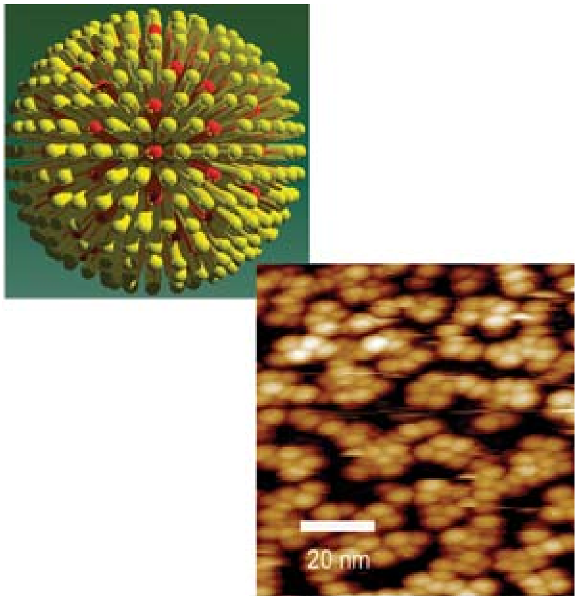

Figure 1: Schematic of ligand-coated gold nanoparticles; (upper left) scanning tunneling microscopy (STM) image of ligand-encapsulated gold nanoparticles showing hexagonal packing.

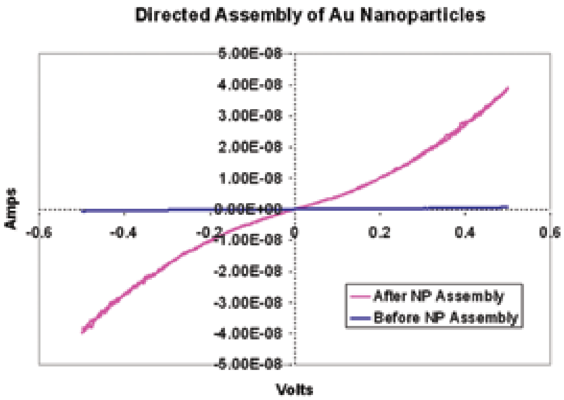

Figure 2: Current-Voltage (I-V) measurements show a 100-times increase in conductivity after the directed assembly of gold nanoparticles in a ~10 nm insulating gap.

Stress Evolution During Growth of Metal Thin Films

R. Moenig, J. Leib, A.R. Takahashi, C.V. Thompson

Sponsorship: NSF

Mechanical stress strongly influences the reliability and performance of highly miniaturized devices, therefore control of stresses in deposited structures and films is of general interest. Obtaining this control requires an understanding of the physical processes involved, as well as a quantitative knowledge of their contributions to total stress of a system. Our work focuses on the stresses that evolve during e-beam evaporative growth of high mobility metals on different amorphous substrates. Figure 1 shows a typical stress curve obtained by measuring substrate bending with a capacitive displacement sensor during film deposition. During early stages, islands nucleate and grow on a surface, causing a compressive stress thought to be related to the surface state of the growing islands [1,2]. As deposition continues, islands begin to coalesce and form a continuous layer. During this process, the stress becomes increasingly tensile while surface energy of the islands is transferred into grain boundary and elastic energy. After the film becomes continuous, the stress reverses and approaches a constant compressive value (again, thought to be related to the state of the film surface during deposition). One possible method of modifying the observed stress thickness behavior is to vary the size of islands using growth interrupts before island coalescence. Figure 2 shows the coarsening of islands during an interrupt which occurs on timescales corresponding to the mobility of an atom on the substrate. Upon resumption of growth the resulting larger islands coalesce at greater thicknesses and therefore lead the tensile peak in Figure 1 to shift towards higher thickness values. Flash depositions of Ta on the surface of deposited films allow for atomic force microscopy imaging of "frozen" films as shown in Figure 2 and provide a method for correlating the island size after a given length of interrupt with corresponding changes in measured stress curves. The ability to lock in a surface state at any stage of deposition or to interrupt growth also provides the means for exploring several other fundamental film stress generators, including the relaxation of stress due to coarsening of grains and islands and due to surface roughness.

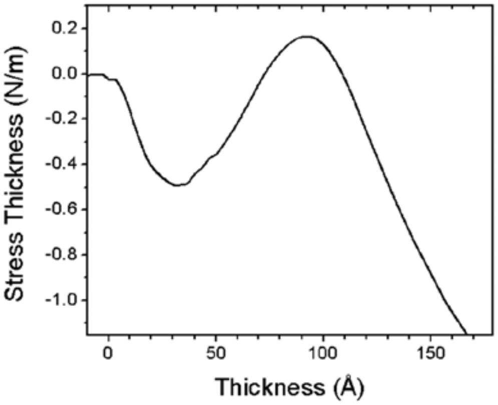

Figure 1: Stress measurement during deposition of Au on borosilicate glass. Deposition occurred at 1 Å/s, substrate was held at RT.

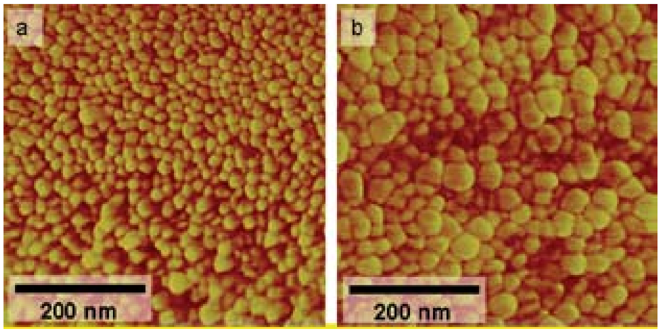

Figure 2: Atomic force microscope phase images of 40 Å Cu films deposited on SiO2. (a) Ta deposition immediately after Cu growth, mean particle diameter 15 nm. (b) Ta deposition 15 min after Cu growth, mean particle diameter 21 nm.

REFERENCES:

[1] Friesen, C., C.V. Thompson, "Reversible Stress Relaxation During Precoalescence Interruptions of Volmer-Weber Thin Film Growth," *Physical Review Letters*, vol. 89, no. 12, p. 126103, 2002.

[2] Friesen, C., C.V. Thompson, "Correlation of Stress and Atomic-Scale Surface Roughness Evolution During Intermittent Homeopitaxial Growth of (111)-Oriented Ag and Cu," *Physical Review Letters,* vol. 93, no. 5, p. 056104, 2004.

Bonding and Boundary Formation Resulting from the Contact of Metallic Nanoclusters

A.R. Takahashi, R. Moenig, J. Leib, C.V. Thompson
Sponsorship: NSF

The properties of ultra-thin metallic films are heavily dependent on the transition from discontinuous islands to continuous films. Additionally, devices assembled from nano-crystallite building blocks are also beginning to show promise for implementing novel applications. In some applications, the nanoclusters must remain isolated from one another, while in other applications, selective electrical contact is required. This research project focuses on the bonding and boundary formation process when nanoclusters are placed in contact with one another. This process is analogous to island impingement during thin film formation. The high surface curvatures of the islands provide a very strong driving force for bonding. An increase in strain energy is compensated by the reduction in surface energy. The intrinsic tensile stress generated by this process is measurable and expected to affect the thin film device properties.

The boundary formation process is being investigated primarily through the use of computer models. These computer models incorporate semi-empirical inter-atomic potentials and molecular dynamics to evolve a system of clusters in time. Through these calculations, we find that the times required for nanometer sized islands to form boundaries can be on the order of nanoseconds (see Figure 1) and that the boundary areas are consistent with predictions from continuum theory. Based on these findings, we are also implementing a finite element model, which incorporates the orientation and contact angle dependencies seen in the atomistic calculations.

In connection with the computational studies, we are using transmission electron microscopy (TEM) to investigate the coalescence and sintering behavior of model systems generated from colloidal suspensions and from pre-coalescence metallic thin films (see Figure 2). Defect structures observed in the TEM will be directly compared to computationally generated defects.

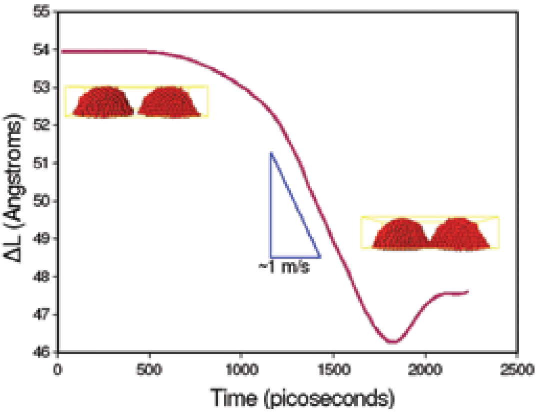

Figure 1: Distance between centers of mass evolution over time showing the completion of the boundary formation process in approximately 2 ns.

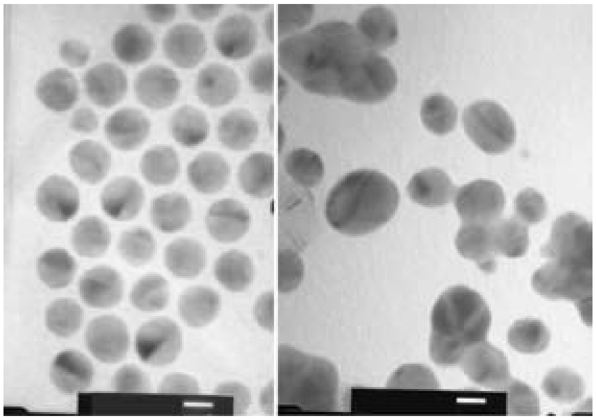

Figure 2: A nanoparticle array before (left) and after (right) heat treatment to induce particle sintering. The scalebars are 10 nm.

Templated Assembly by Selective Removal

S. Jung, F. Eid, C. Livermore

Sponsorship: NSF, 3M

In this project, an effective technique for site-selective, multicomponent assembly on the nano- and microscale has been developed. Creation of practical nanosystems using this technique is underway. This approach offers great promise for assembling arbitrary (not necessarily periodic) systems of different types of nanoscale components, such as electronics (memory, logic, interconnects, displays) and sensor systems.

The key elements of the approach are as follows. First, the topography of the substrate is modified to match the components' 3D shapes. Then, the substrate and components are coated with an adhesion promoter, such as a hydrophobic SAM, for adhesion in a water-based environment. The components and substrate are placed in a fluid environment for the assembly process then megahertz-frequency ultrasound is applied to the fluid bath. Components contact the substrate randomly and adhere wherever they land; however, components that are not in shape-matched sites are removed by fluid forces initiated by the high-frequency ultrasound. Components in shape-matched sites are selectively retained because their adhesive force is stronger than the removal forces. Figure 1 is an optical micrograph showing the successful assembly of 1.6 µm diameter microparticles into designated sites on the substrate. Figure 2 shows how measured assembly yield of microparticles into holes of slightly different sizes increases with the contact area between particles and substrate.

This approach to assembly is inherently selective. Since each component will adhere only in a shape- and size-matched site, geometrically distinct components will assemble only into their designated assembly sites. Therefore, the organizing information is allowed to be stored in the template initially, and components that may not be compatible with top-down manufacturing techniques can be added to the system later, with high positional precision. Work is in progress to demonstrate this approach in smaller- size scales and to create practical nanosystems using this technology.

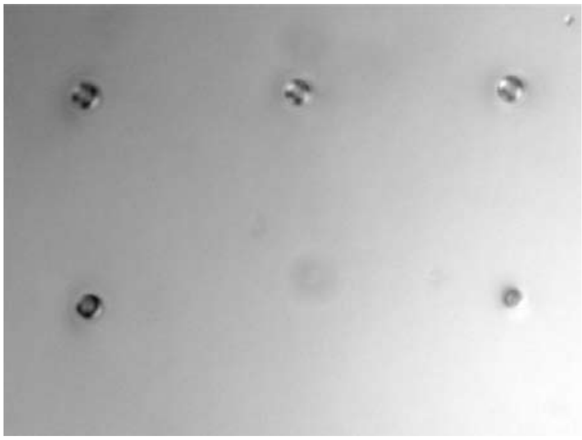

Figure 1: Optical micrograph showing four particle-filled holes and one empty hole.

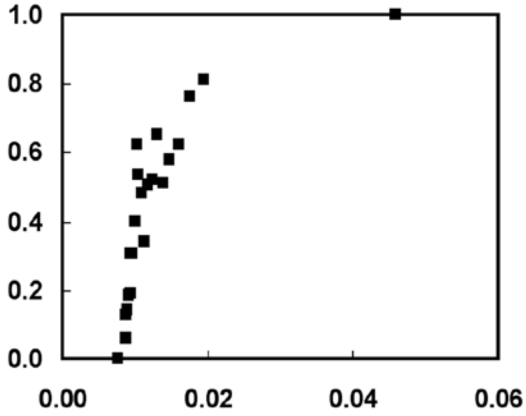

Figure 2: Plot of assembly yield (number of particle-filled holes/total number of holes) vs. contact area between particle and hole. Assembly yield increases from 0% to 100% as quality of the shape match improves.

Block Copolymer Lithography

F. Ilievski, G.J. Vancso, C.A. Ross, H. Smith, E.L. Thomas

Sponsorship: NSF, CMSE

Fabrication of large-area periodic nanoscale structures using self-organizing systems is of great interest because of the simplicity and low cost of the process. Block copolymers consist of polymer chains made from two chemically distinct polymer materials. The chains can self-assemble to form small-scale domains whose size and geometry depend on the molecular weights of the two types of polymer and their interaction [1]. The domains have a very uniform distribution of sizes and shapes. We have been using block copolymers as templates for the formation of structures such as magnetic particles, by selectively removing one type of domain and using the resulting template to pattern a nanostructured magnetic film. An example is shown in Figure 1, where perpendicularly magnetic CoCrPt dots have been made using ion milling to pattern a CoCrPt film. The dots maintain the out-of-plane magnetization of the film, and the out-of-plane coercivity of the array is increased tenfold as compared to the as-deposited film (Figure 2). Additionally, the magnetic switching volume of the array is approximately equal to the physical volume of one dot, suggesting that the dots are magnetically as well as physically decoupled and switch coherently. The patterning process has been successfully applied to the fabrication of magnetic dots from Co, NiFe^2 and multilayer CoFe/Cu/NiFe films. The arrays of Co and NiFe dots show strong magnetostatic interactions and exhibit collective switching of 2-6 dots [2]. The multilayer dots maintain the magnetoresistance present in the as-deposited multilayer film. Furthermore, the separate reversal of the two magnetic layers is visible in both patterned and unpatterned films [3]. Work is now concentrated on producing ordered arrays with perpendicular magnetization by templating the block copolymer using shallow grooves for storage media applications.

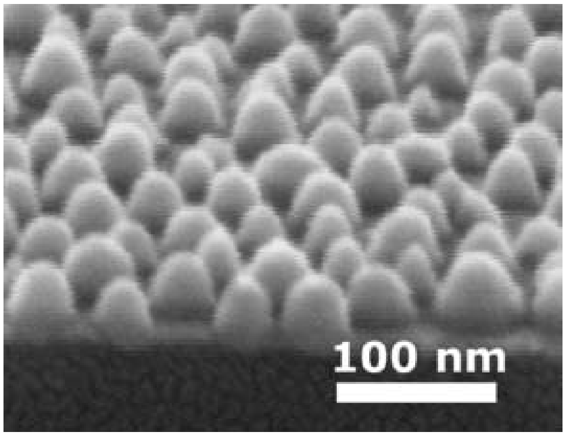

Figure 1: Tilted Scanning Electron Micrograph cross-section of a 15 nm thick CoCrPt dot array. The magnetic particles appear taller than the CoCrPt film thickness due to the presence of a W-etch mask capping each particle.

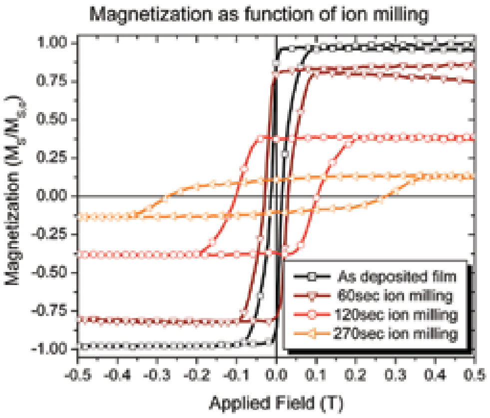

Figure 2:The out-of-plane magnetization curves for the sample shown in Figure 1 as a function of the ion-milling step. The moment has been normalized to the moment of the as-deposited film and it decreases monotonously as material is removed. The coercivity increases due to separation of the film in separate domains.

REFERENCES:

[1] Thomas, E.L., R.L. Lescanec, "Phase Morphology in Block Copolymer Systems," *Philosophical Transactions: Physical Sciences and Engineering,* vol. 348, no. 1686, pp.149-164, 1994.

[2] Cheng, JY., C.A. Ross, "Magnetic Nanostructures from Block Copolymer Lithography: Hysteresis, Thermal Stability and Magnetoresistance," *Physical Review B: Condensed Matter and Materials Physics,* vol. 70, no. 6, pp. 064417: 1-9, August 2004.

[3] Ross, C.A., F.J. Castaño, E. Rodriguez, S. Haratani, B. Vögeli, H.I. Smith, "Size-Dependent Switching of Multilayer Magnetic Elements," *Journal of Applied Physics*, vol. 97, no. 5, pp. 053902: 1-6, 2005.

Proximity Effects in Self-organized Binary Particle-block Copolymer Blends

M.R. Bockstaller, E.L. Thomas

Sponsorship: ARO, Alexander von Humboldt Foundation

Depending on the surface chemistry of gold nanocrystals of equal metal core size, two morphological types of self-organized block copolymer–particle blends are observed: (1) the segregation of the nanocrystals to the interfacial areas; or (2) the preferential uniform distribution within one of the respective polymer domains. The confinement of the nanocrystals to the narrow interfacial regions of the microstructure in type one blends results in high local particle filling fractions and gives rise to electromagnetic coupling upon light irradiation, accompanied by a pronounced increase in absorbance.

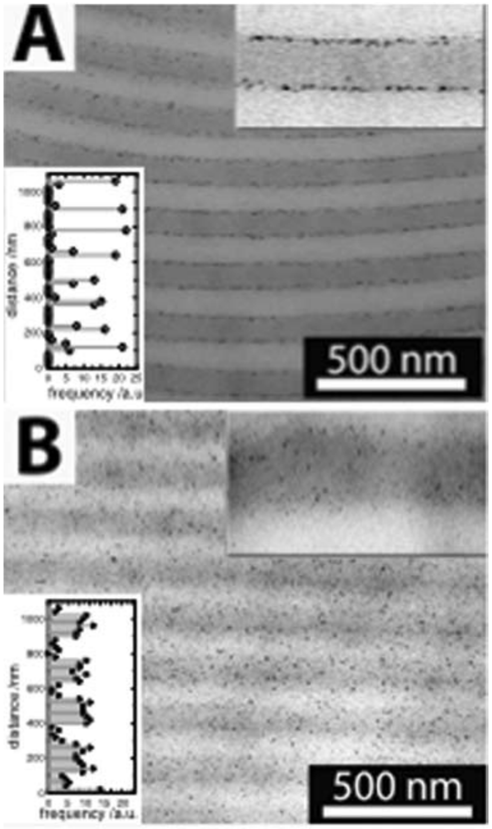

Figure 1: Bright field transmission electron micrographs of the unstained block copolymer/nanocrystal composite material after microsectioning *normal* to the layer direction demonstrating particle deposition at the IMDS (PS-PEP/$AuSC_{12}H_{25}$, type 1) in panel A, and homogeneous selective-layer morphology (PS-PEP/AuSPS, type *U*) in panel B, respectively. PEP domains appear as brighter regions in the micrograph. The volume-filling fraction of gold for both samples is $\phi \cong 0.01$. The lower insets in panel A and B depict the respective particle frequencies in 001 direction obtained by particle counting in equally sized area elements of 20 nm width. In panel B, a small amount of tilt of the IMDS with respect to the electron beam direction results in a somewhat smeared appearance of the PS-PEP interface.

Templated Self-Assembly of Nanoporous Alumina: A Wafer-level Methodology for Ordered and Aligned Nanostructures (Nano-wires, -rods, -dots and -tubes)

R. Krishnan, J. Oh, B. Hsu, C.V. Thompson

Sponsorship: MARCO IFC, SMA, NSF

Nano-sized materials are core building blocks for advanced functional devices, such as interconnects, logics, memories, sensors, and displays. Due to their size-sensitive electrical, optical, magnetic and chemical properties, fabricating these devices with controlled size and distribution on the device-applicable substrates is of importance. As a strategy, we are developing templated self-assembly methods that combine top-down (lithography) and bottom-up (self-assembly) approaches for fabricating and assembling metallic nano-wires, -rods, and -dots for new applications including nano-contacts for devices and interconnects for mixed-material and multifunctional micro- and nano-systems.

Anodic aluminum oxide (AAO) is a self-ordered, nano-structured material that is well-suited for use as a template in magnetic, electronic and opto-electronic devices. Under proper anodization conditions, aluminum oxidizes as a porous structure with aligned pores that have close-packed (hexagonal) order at short range and with pore sizes that can be varied from 4 nm-300 nm. The excellent mechanical and thermal stability of porous alumina makes it suitable both as physical masks for deposition of nanodot catalysts, as well as a supporting template for catalyzed growth of semiconductor nanowires and carbon nanotubes. While short-range pore ordering can be achieved during anodization, domains (<5 μm) of different repeat directions, which occur at longer ranges, limit further implementation of novel devices. We have developed a technique to obtain single-domain, porous alumina with sub-30 nm pore diameter and high aspect ratio (>50:1) on silicon substrates [1]. Anodization of aluminum films deposited on substrates with lithographically defined periodic topography lead to templated self-assembly of alumina pores that are perfectly ordered over large areas. The template controls the pore spacing and ordering symmetry, while the anodization conditions independently control the pore diameters to sub-lithographic length scales. Topographic templating of long-range order in AAO allows independent control of the pore size, spacing, and order symmetry in ranges not achievable without templating. Using the perfectly-ordered AAO templates, we have fabricated ordered metallic nanodots, nanorods, and nanotubes as well as well-aligned, multi-walled carbon nanotubes on silicon [2]. We are exploring the use of metal/CNT-filled alumina templates as electrical nano-breadboards using dip-pen nanolithography for applications in molecular electronics. These results demonstrate a wafer-scale approach to the control of the size, pitch, ordering symmetry, and position of nanomaterials in a rigid insulating scaffold.

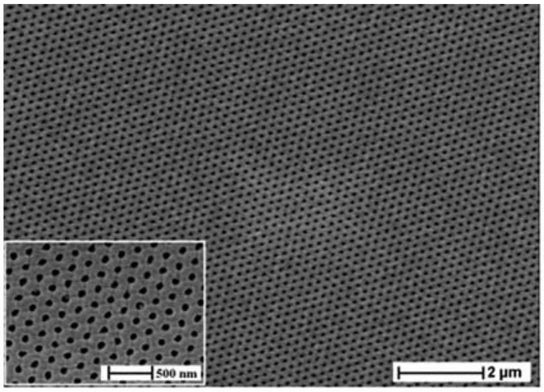

Figure 1: Scanning electron micrograph of perfectly ordered porous alumina with hexagonal symmetry on silicon over wafer-scale areas with pore diameter of 80 nm and pore spacing of 180 nm [1].

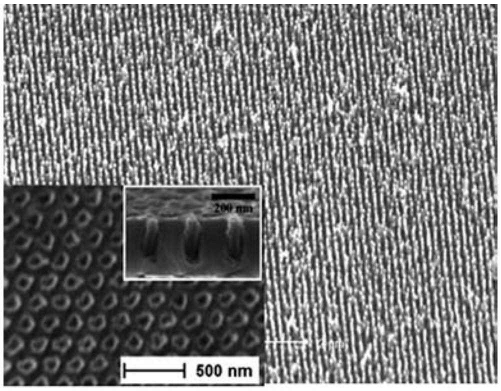

Figure 2: Scanning electron micrograph of ordered and well-aligned carbon nanotube arrays on silicon. Inset shows aligned CNT arrays in ordered porous alumina after ion-milling the surface [2].

REFERENCES:

[1] Krishnan, R., K. Nielsch, C.A. Ross, H.I. Smith, C.V. Thompson, "Ordered Single-Domain Alumina Nanopore Arrays and Metallic Nanowire Arrays on Silicon for On-Chip Integration of Semiconductor Devices," *204th Meeting of the Electrochemical Society*, Orlando, FL, October 2003.

[2] Krishnan, R., H.Q. Nguyen, C.V. Thompson, W.K. Choi, Y.L. Foo, "Wafer-level Ordered Arrays of Aligned Carbon Nanotubes with Controlled Size and Spacing on Silicon," *Nanotechnology*, vol.16, no. 6, pp. 841-845, Jun. 2005.

Templated Self-Assembly of Metal Particles: Controlled Dewetting of Thin Films

A.L. Giermann, C.A. Ross, H. Smith, C.V. Thompson

Sponsorship: NSF

We are exploring templated self-assembly (TSA) as a tool for producing ordered arrays of metal nanodots over large areas via dewetting of thin solid films. Such arrays may be interesting in memory or plasmonic applications, and for use as catalysts for the growth of carbon nanotube or semiconductor nanowire arrays.

TSA is an attractive tool for patterning nano-scale materials. Use of physical templates to alter the surface environment can initiate self-forming and self-ordering processes in materials systems that have little or no inherent order. TSA is particularly attractive if we can obtain sub-lithographic assembly, or assembly of objects with sub-lithographic sizes.

As an initial demonstration of templated dewetting, we achieved one-to-one self-assembly of gold particles less than 100 nm in diameter and ordered over large areas [1]. We deposited gold films on di-periodic arrays of pits on oxidized silicon substrates, thereby modulating the curvature of the films and generating a well-ordered solid-state dewetting process. Compared to dewetting on flat substrates, the templates impose a significant decrease in average particle size, as well as ensure a narrow size and spatial distribution (Figure 1). This templating technique uniquely results in crystallographic ordering (i.e., graphoepitaxy) of the particles, imposing an in-plane texture, and changing the out-of-plane texture (Figure 2). Particles formed in topographic features are expected to be stable with respect to agglomeration during tube or wire growth.

Our current efforts include investigating the templating phenomena in other metals, particularly those that are known to catalyze nanotube and nanowire growth. We are also exploring methods for further scaling down the process and seeking topographies that will enable self-assembly on sub-lithographic length scales. In addition, we are developing phase field and numeric models of topographic dewetting in order to fully characterize the mechanism.

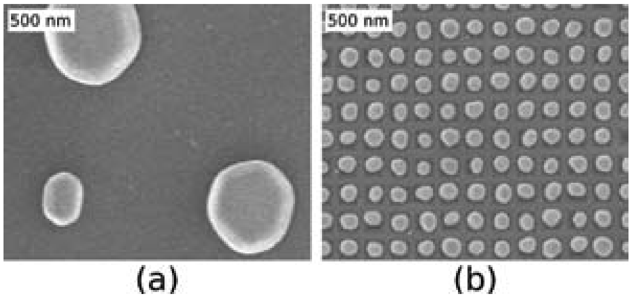

Figure 1: The effect of topography on particle morphology. The results of dewetting a 21 nm thick Au film on (a) a flat substrate and (b) a topographic substrate. Micrographs are displayed at the same magnification to emphasize the effect of topography on particle size. Scale bars are 500 nm in length.

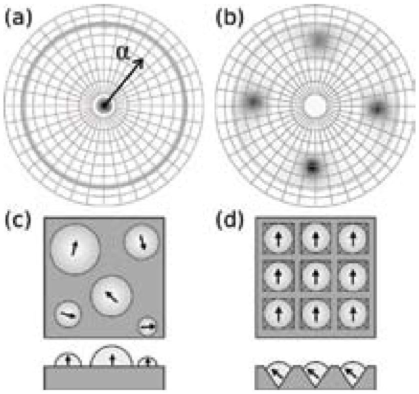

Figure 2: The effect of topography on particle orientation. (a) and (b) show Au (111) X-ray pole figures ($37.4^\circ < 2\theta < 38.6^\circ$), (a) for particles on a flat substrate and (b) for particles on a topographic substrate. (c) and (d) schematically illustrate the particle orientation on flat and topographic substrates, respectively. The arrows indicate the (111) projection.

REFERENCES:

[1] Giermann, A.L., C.V. Thompson, “Solid-State Dewetting for Ordered Arrays of Crystallographically Oriented Metal Particles,” *Applied Physics Letters*, vol. 86, p. 121903, March 2005.

Templated Self-Assembly

J.Y. Cheng, H. Smith, A.M. Mayes, C.A. Ross

Sponsorship: NSF

Self-organized materials have been used to pattern large-area nanometer-scale periodic structures. However, typical self-assembled materials have only short-range ordered limiting their usefulness in nanodevices. With the guidance of lithographically defined templates, the templated self-assembly (TSA) method creates high-precision and high-density nanostructures by combining advantages of both self-assembled materials and lithography techniques. Templates made from electron-beam lithography have been employed to study TSA effect of block copolymers. Based on a simple free energy model describing the layering behavior of block copolymers in a one-dimensional topographical confinement (Figure 1a) and experimental data (Figure 1b), we are able to predict the design window (Figure 2a) for templates to make a particular arrangement of polymer domains (Figure 2b). The understanding of templated self-assembled block copolymers will facilitate the design of hybrid systems combining top-down and bottom-up processing, enabling new nanofabrication technologies based on these self-assembling materials.

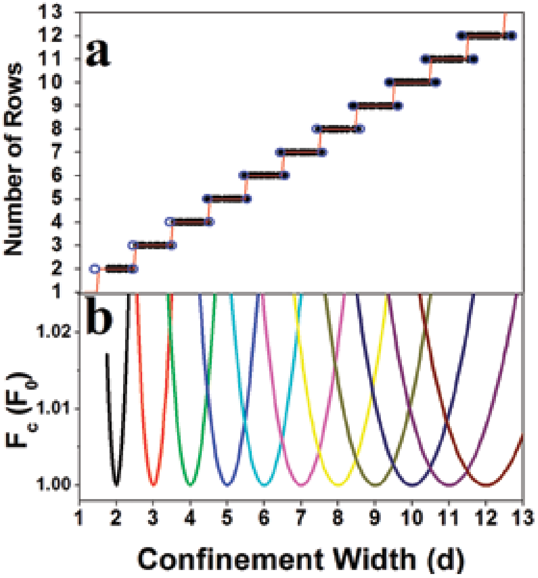

Figure 1: (a) The number of rows in the groove, *N,* vs. confinement width, *W*, showing the widths at which arrays with *N* rows are stable. (b) Energy vs. confinement width of block copolymer system. The confined block copolymer system, of given *W,* will ideally select the value of *N* with the lowest free energy. A transition in the number of rows from *N* to *N*+1 occurs when $W \sim (N+0.5)d$, in agreement with the experimental data of Figure 1(a).

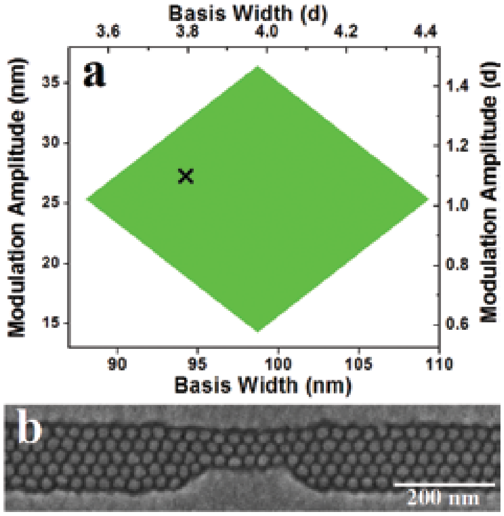

Figure 2: The creation of a specific block copolymer array geometry using a modulated template. (a) The modulation conditions that are expected to produce an array consisting of 5*p*-long 3-row arrays interspersed with 20*p*-long 5-row arrays. (b) Scanning electron micrograph of a section of an ordered array with 3 and 5 rows of domains, created using a template with dimensions indicated with a cross on part a.

REFERENCES:

[1] Cheng, J.Y., A.M. Mayes, C.A. Ross, "Nanostructure Engineering by Templated Self-Assembly", *Nature Materials*, vol. 3, no. 11, pp. 823-828, November 2004.

[2] Cheng, J.Y., C.A. Ross, E.L. Thomas, H.I. Smith, G.J. Vancso "Templated Self-Assembly of Block Copolymers: Effect of Substrate Topography", *Advanced Materials*, vol. 15, no. 19, pp. 1599-1602, October 2003.

Nanofabricated Diffraction Gratings

C.-H. Chang, R.C. Fleming, R.K. Heilmann, J. Montoya, M.L. Schattenburg, H. Smith

Sponsorship: NASA, XOPT, Inc., Plymouth Grating Laboratory

Diffraction gratings and other periodic patterns have long been important tools in research and manufacturing. Grating diffraction is due to the coherent superposition of waves—a phenomena with many useful properties and applications. Waves of many types can be diffracted, including visible and ultraviolet light, X-rays, electrons, and even atom beams. Periodic patterns have many useful applications in fields such as optics and spectroscopy, filtering of beams and media, metrology, high-power lasers, optical communications, semiconductor manufacturing, and nanotechnology research in nanophonics, nanomagnetics and nanobiology.

The performance of a grating is critically dependent on the geometry of individual grating lines. Lines can have rectangular, triangular, or other geometries, depending on the application. High efficiency requires control of the geometric parameters that define individual lines (e.g., width, height, smoothness, sidewall angle, etc.) in the nanometer or even sub-nanometer range. For some applications, control of grating period in the picometer to femtometer range is critical. Traditional methods of fabricating gratings, such as diamond tip ruling, electron and laser beam scanning, or holography, generally result in gratings that fall far below theoretical performance limits due to imperfections in the grating line geometry. The main goal of our research is to develop new technology for the rapid generation of general periodic patterns with control of geometry measured in the nanometer to sub-nanometer range in order to achieve near-theoretical performance and high yields.

The fabrication of gratings is generally accomplished in two main steps: (1) lithographic patterning into a photosensitive polymer resist; and (2) pattern transfer. A companion research program in this report entitled *Advanced Interference Lithography Technology* describes progress in advanced grating patterning technology. In this section, we report on research in pattern transfer technology. The development of a variety of grating geometries and materials is ongoing. Advanced gratings have been fabricated for ten NASA missions, and further advances are sought for future missions [1]. Figure 1 depicts a gold wire-grid transmission grating designed for filtering deep-UV radiation for atom telescopes, while Figure 2 depicts a nano-imprinted saw tooth reflection grating for X-ray spectroscopy.

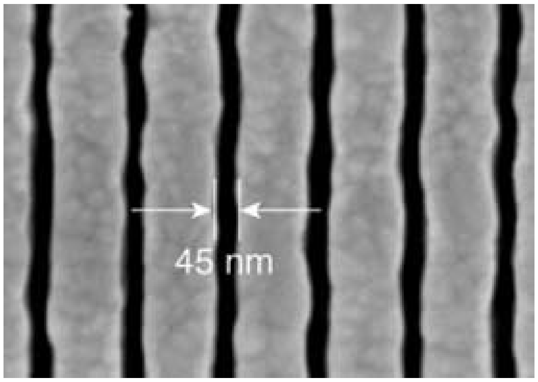

Figure 1: Scanning electron micrograph of a deep-UV blocking grating used in atom telescopes on the NASA *IMAGE* and *TWINS* missions. The grating blocks deep-UV radiation while passing energetic neutral atoms.

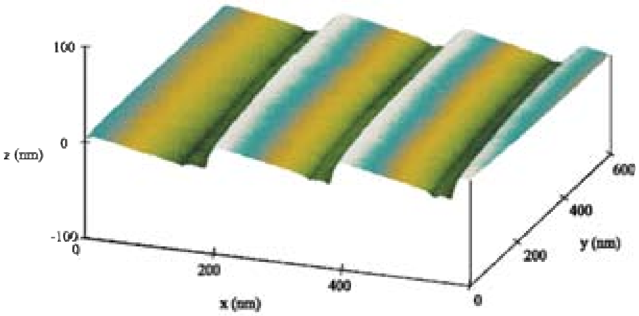

Figure 2: Atomic force microscope image of -200 nm-period thermal-nano-imprint grating with 7° blaze angle developed for the NASA *Constellation X* mission. The grooved surfaces are extremely smooth with a root mean square (RMS) surface roughness of <0.2 nm.

REFERENCES:

[1] Schattenburg, M.L., "From Nanometers to Gigaparsecs: The Role of Nanostructures in Unraveling the Mysteries of the Cosmos," *Journal of Vacuum Science Technology B*, vol. 19, no. 6, pp. 2319-2328, November 2001.

Advanced Interference Lithography Technology

C.-H. Chang, R.C. Fleming, R.K. Heilmann, J. Montoya, M.L. Schattenburg, Y. Zhao

Sponsorship: NASA, Plymouth Grating Laboratory

Traditional methods of fabricating gratings, such as diamond tip ruling, electron and laser beam scanning, or holography, are generally very slow and expensive, and they result in gratings with poor control of phase and period. More complex periodic patterns, such as gratings with chirped or curved lines, or 2D and 3D photonic patterns, are even more difficult to pattern. This research program seeks to develop advanced interference lithography tools and techniques to enable the rapid patterning of general periodic patterns with much lower cost and higher fidelity than current technology.

Interference lithography (IL) is a maskless lithography technique based on the interference of coherent beams. Interfering beams from an ultra-violet laser generate interference fringes that are captured in a photo-sensitive polymer resist. Much of the technology used in modern IL practice is borrowed from technology used to fabricate computer chips. Traditional IL methods result in gratings with large phase and period errors. We are developing new technology based on interference of phase-locked scanning beams, called scanning beam interference lithography (SBIL). The SBIL technique has been realized in a tool called the MIT Nanoruler (Figure 1), which recently won an R&D 100 award. By using the Nanoruler, large gratings can be patterned in a matter of minutes, with a grating phase error of only a few nanometers and a period error in the ppb range (Figure 2). Current research efforts seek to generalize the SBIL concept to pattern more complex periodic patterns, such as variable period (chirped) gratings, 2D metrology grids, and photonic patterns [1]. Important applications of large, high fidelity gratings include high-resolution X-ray spectrometers on NASA X-ray astronomy missions, high-energy laser pulse compression optics, and length metrology standards.

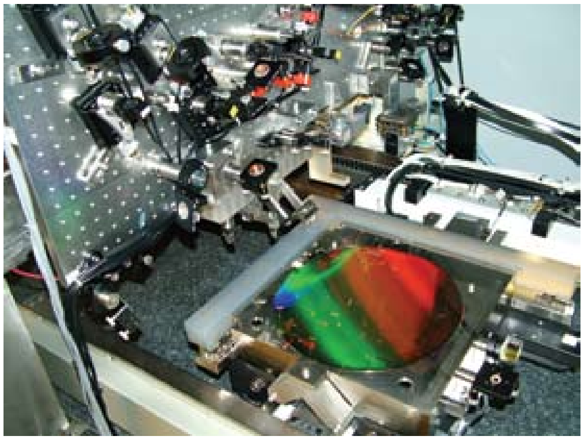

Figure 1: Photograph of the Nanoruler lithography and metrology system built by MIT students. This unique tool is the most precise grating, patterning, and metrology system in the world.

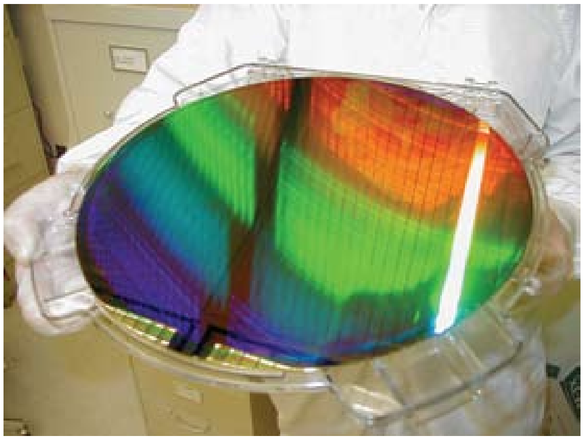

Figure 2: A 300 mm-diameter silicon wafer patterned with a 400 nm-period grating by the Nanoruler. The grating is diffracting light from the overhead fluorescent bulbs.

REFERENCES:

[1] Pati, G.S., R.K. Heilmann, P.T. Konkola, C. Joo, C.G. Chen, E. Murphy and M.L. Schattenburg, "Generalized Scanning Beam Interference Lithography System for Patterning Gratings with Variable Period Progressions," *Journal of Vacuum Science & Technology B: Microelectronics and Nanometer Structures*, vol. 20, no. 6, pp. 2617-2621, November 2002.

An Approach to Realizing Index Enhancement without Absorption for Immersion Lithography

V. Anant, M. Rådmark, T.C. Killian, K.K. Berggren

Sponsorship: AFOSR

In this work, we propose and evaluate a scheme for refractive index enhancement that achieves the following objectives: (1) an index of refraction greater than unity in an atomic vapor; and (2) optical amplification rather than absorption of the propagating probe beam. The scheme achieves the first of these objectives by tuning the probe beam close to an atomic resonance. The second is achieved by using an additional incoherent optical pump beam that inverts population between the two levels with which the near-resonant probe beam interacts. This scheme is simple and is shown to be tolerant to temperature-related broadening effects. However, it is susceptible to intensity-related broadening effects and background noise, due to amplified spontaneous emission. Such a scheme may find applications in the fields of immersion microscopy and immersion photolithography, where the high-index material could replace lower-index immersion liquids, as well as in applications such as all-optical switching, where an optically controlled refractive index is desirable.

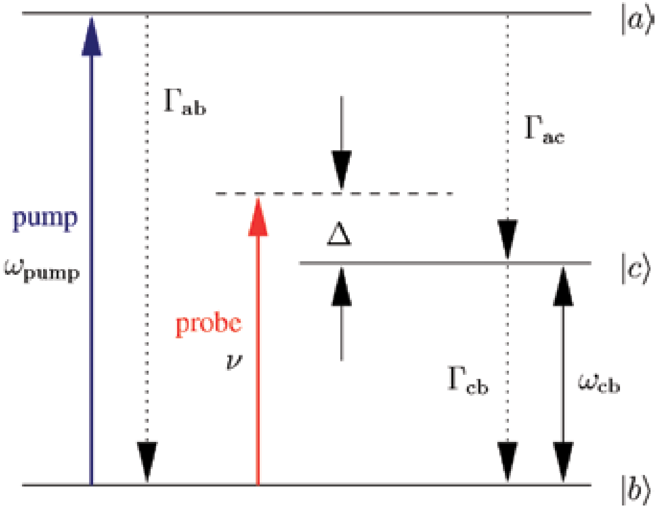

Figure 1: Energy level diagram showing incoherent decay rates and driving fields for the index-enhanced medium. A two-level system with ground state |*b*> and excited state |*c*> interacts with a coherent oscillating electromagnetic probe field at frequency *ν* detuned by Δ from the energy difference (ω_{cb}) between |*c*> and |*b*>. An incoherent oscillating electromagnetic pump field at frequency $\omega_{pump} = \omega_{ab}$ promotes population from |*b*> to upper lying level |*a*>. |*a*> is an upper level that decays at rate Γ_{ac} to level |*c*>.

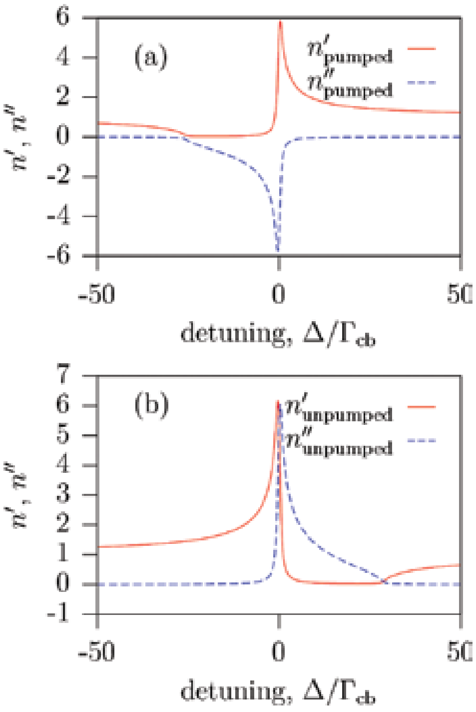

Figure 2: Plot of the refractive index n'' and absorption coefficient n'' as a function of Δ for the 4^1S_0 to 4^1P_1 transition in Ca: (a) pumped case, and (b) un-pumped case. For the pumped case, we see that $n'' < 0$, resulting in amplification (rather than absorption) of the probe laser. The maximum value of n' occurs slightly off resonance ($n_{max} \approx 6$ at $\Delta \approx 0.3\Gamma_{cb}$).

Sub-Resolution Lithography Using Quantum State Quenching

M. Rådmark, K.K. Berggren
Sponsorship: MIT

A way to improve spot size and resolution in optical projection lithography has been demonstrated in atomic beams using quantum state quenching near the node of an optical field [1]. Recently an extension of this technique has been proposed to directly control the exposure of photo-resist molecules [2]. The exposure sequence consists of three steps. In the first step, a diffraction-limited spot of the photo-resist would be excited. Immediately thereafter, a second incident pulse containing a node at its center would quench the outer parts of this spot, decreasing the spot size below the diffraction limit. In the third step, the remaining excited molecules would react to expose the resist.

To obtain the node in the quenching pulse, one could let the driving field of this pulse be a standing wave. A key property of this standing wave is that its maximum intensity should be much higher than the saturation intensity for de-excitation. With such a high intensity, the region where the intensity of the standing wave is too low to effectively quench excited molecules will be very narrow, and the remaining excited spot will be much smaller than the diffraction limit. The distribution of excited molecules, after quenching by the second pulse, will depend on the intensity of this pulse. Figure 1 shows calculations of point spread functions (PSFs) given by a quenching pulse with a standing wave of different intensities as driving field. With a wavelength of the standing wave on the order of 400 nm and a high maximum intensity (~ 10 W/μm^2), the PSF of excited molecules could be made very narrow and spot sizes on the order of tens of nanometers could possibly be achieved. Such a narrow PSF could be applied to achieve continued scaling of optical lithography into the sub-50-nm regime.

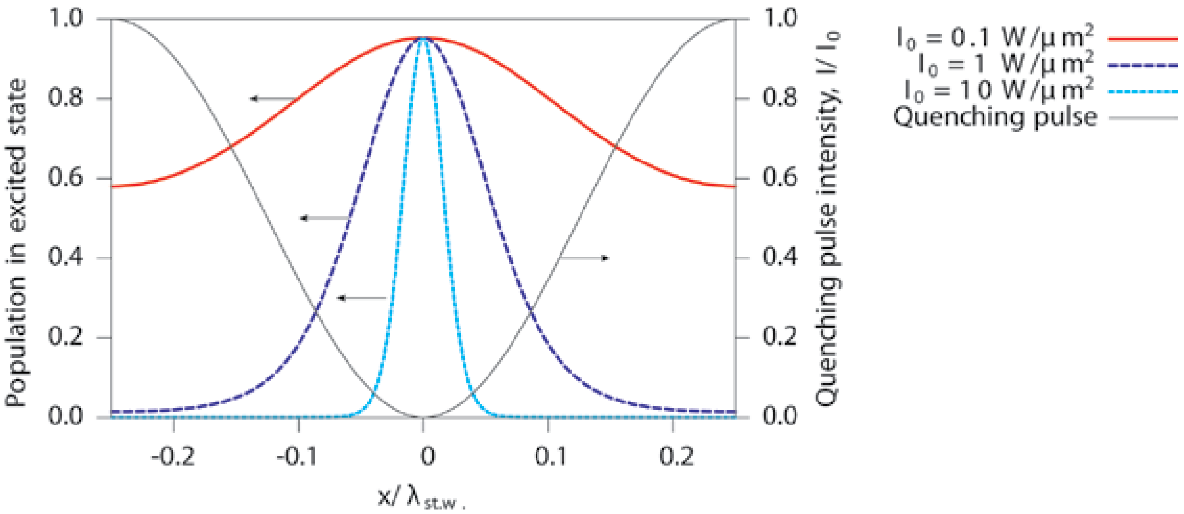

Figure 1: Distribution of molecules in the excited state, after the effects of a quenching pulse. The I_0 is the maximum intensity of the quenching pulse and $\lambda_{st.w}$ is the wavelength of the standing wave. The molecular cross-section for stimulated emission is assumed to be 10^{-16} cm^2. The higher the intensity of the quenching pulse, the more effectively it will quench excited molecules around the node, leading to a narrower PSF.

REFERENCES:

[1] Chu, A.P., K.K. Berggren, K.S. Johnson, M.G. Prentiss, "A Virtual Slit for Atom Optics and Nano-lithography," *Quantum and Semiclass Optics, Journal of the European Optical Society Part B*, vol. 8, no. 3, pp. 521-530, June 1996.

[2] Hell, S.W., "Strategy for Far-field Optical Imaging and Writing without Diffraction Limit," *Physics Letters A*, vol. 326, no. 1-2, pp. 140-145, May 2004.

Fabrication Methods for Adiabatic Quantum Computing Devices

B. Cord, W. Kaminsky, T.P. Orlando, K.K. Berggren

Sponsorship: Quantum Computing Graduate Research Fellowship, AFOSR

Adiabatic quantum computing devices (AQCs) have been implemented successfully in several types of systems, including ion traps, nuclear spins, and photon cavities. However, we find implementing AQCs in superconductive circuits offers several key advantages. Primarily, using standard techniques adapted from the semiconductor industry, we can fabricate very large numbers of superconductor-based qubits in CMOS-compatible materials, [1].

The stringent resolution and uniformity requirements for AQC devices present an interesting fabrication challenge. In order to perform certain AQC experiments, Josephson junctions with diameters of ~ 50 nm are useful. While previous quantum computing experiments at MIT used devices fabricated using optical projection lithography, sub-100 nm dimensions require alternate techniques, such as electron-beam lithography and suspended shadow-mask evaporation. Additionally, the uniformity of these nanoscale junctions must be high and the areas of the Josephson junctions within a single device must exhibit very low variation.

No readily-available lithographic technology meets these requirements, so research is being conducted on methods of defining arbitrary features as small as 50 nm with the precision required for adiabatic quantum computing. Current experiments have focused on improving the resolution and uniformity of the scanning electron-beam lithography (SEBL) system in the Nanostructures Laboratory, particularly in investigating the effects of different pattern geometries on the uniformity of very small features. Parallel work is also being done on a reliable, automated method of measuring the dimensions of very small structures for the purposes of determining uniformity, using scanning electron microscope (SEM) images and image-processing software.

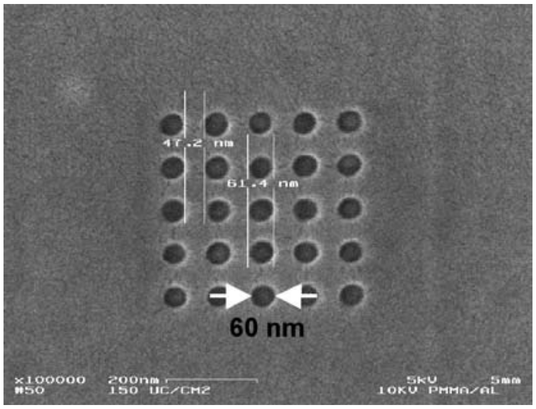

Figure 1: SEM of an array of 60nm diameter features in photoresist

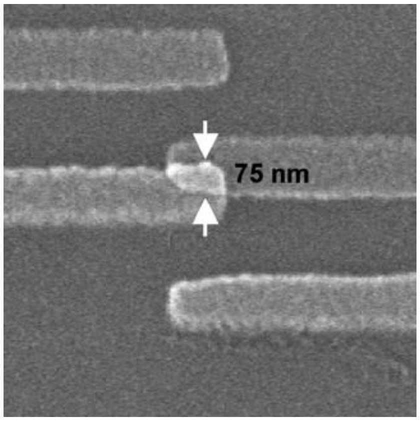

Figure 2: SEM of an 0.007μm^2 Al/AlO$_x$/Al Josephson junction fabricated via shadow-mask evaporation

REFERENCES:

[1] Berggren, K.K., “Quantum Computing with Superconductors,” *Proceedings of the IEEE,* vol. 92, no. 10, pp. 1630-1638, October 2004.

Superconducting Persistent Current Qubits in Niobium

Y. Yu, J. Habif, D. Nakada, J.C. Lee, D. Berns, B. Cord, T.P. Orlando, K.K. Berggren, L. Levitov, S. Lloyd,
in collaboration with S. Valenzuela, M. Tinkham (Harvard)
Sponsorship: DURINT, ARDA

Quantum Computation combines the exploration of new physical principles with the development of emerging technologies. We are beginning this research with the hope to accomplish the manipulation, control, and measurement of a single two-state quantum system, while maintaining quantum coherence between states. This process requires a coherent two-state system (a qubit) along with a method for control and measurement. Superconducting quantum computing could accomplish this in a manner that can be scaled to a large numbers of qubits. We are studying the properties of a two-state system made from a niobium (Nb) superconducting loop, which can be incorporated on-chip with other superconducting circuits for control and measurement. The devices we study are fabricated at MIT Lincoln Laboratory, which uses a Nb-trilayer process for the superconducting elements and optical projection photolithography to define circuit features. While our system is inherently scalable, we are challenged to demonstrate appreciable quantum coherence.

The particular device under study is made from a loop of Nb interrupted by three Josephson junctions (Figure 1a). The application of an external magnetic field to the loop induces a circulating current whose magnetic field either enhances (circulating current in the clockwise direction) or diminishes (counterclockwise) the applied magnetic field. When the applied field is near one-half of a flux quantum Φ_0, quantum superposition of both the clockwise and counterclockwise current states is possible. Thus the system behaves as a two-state system. The potential energy versus circulating current is a so-called double-well potential, with the two minima representing the two states of equal and opposite circulating current as shown in Figure 1c. The flux produced by the circulating currents can be measured by the sensitive flux meter provided by the dc SQUID.

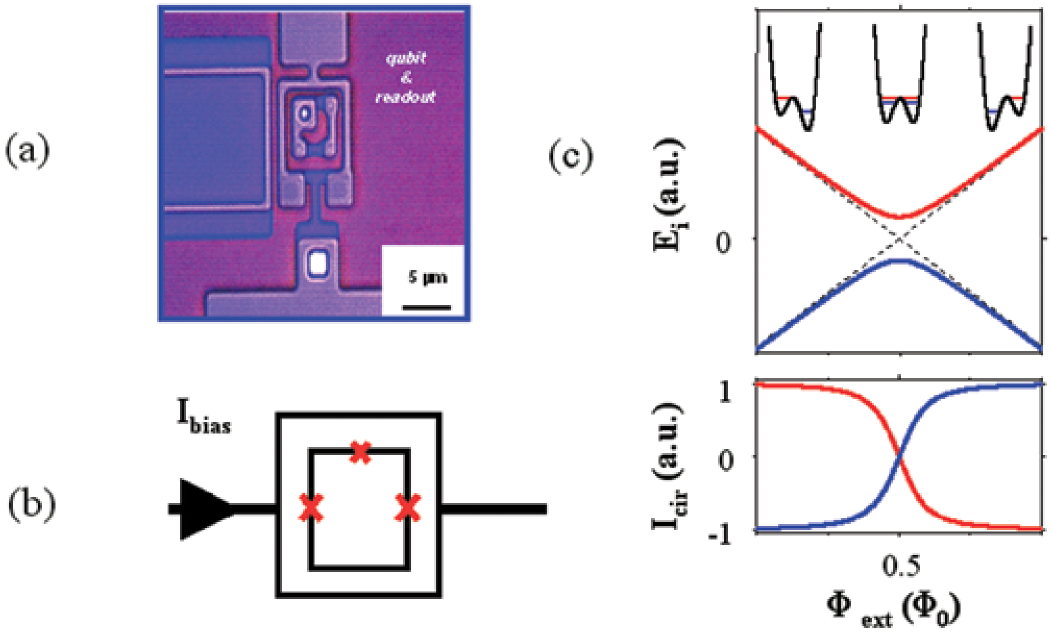

Figure 1: (a) Scanning electron microscope image of the persistent current qubit (inner loop) surrounded by the measuring dc SQUID. (b) a schematic of the persistent current qubit and measuring SQUID; the x's mark the Josephson junctions. (c) the energy levels for the ground state (dark line) and the first excited state of the qubit versus applied flux Φ_{ext}. The double well potentials are shown schematically in the above graph. The lower graph shows the circulating current in the qubit for both states as a function of applied flux (in units of flux quantum Φ_0).

Rapid Measurements in Superconducting Persistent Current Qubits

Y. Yu, W.D. Oliver, T.P. Orlando

Sponsorship: DURINT, ARDA

We installed a rapid measurement setup with a band width of about 1 GHz on a dilution refrigerator. By using an ultra-fast measurement scheme, we investigated the spectroscopy of superconducting Nb persistent current (PC) qubits. The time-resolved experiments showed that the energy relaxation time between the macroscopic quantum states is about 10 μs [1, 2]. We also demonstrated the superposition of macroscopic quantum states and Rabi oscillations between two macroscopic quantum states with microwave irradiations. The long-time macroscopic quantum coherence, together with the advanced fabrication technique, suggests the strong potential of realizing the quantum computing with Nb-based superconducting qubits.

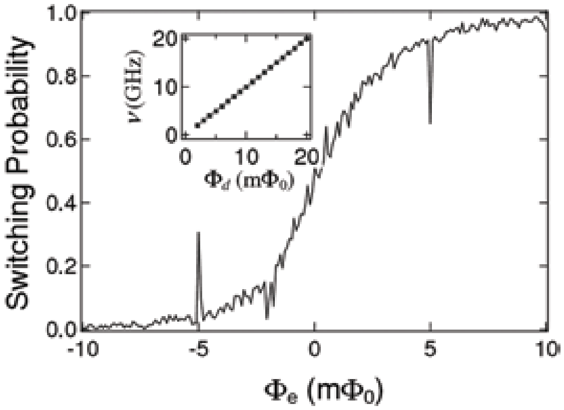

Figure 1: Switching probability vs. external magnetic field with 10 GHz microwave irradiation. The resonant peak and the dip are caused by photon induced transition between two macroscopic quantum states. Inset: microwave frequency vs. the distance between the peak and the dip (symbols). The solid line is the theoretical calculation using qubit parameters.

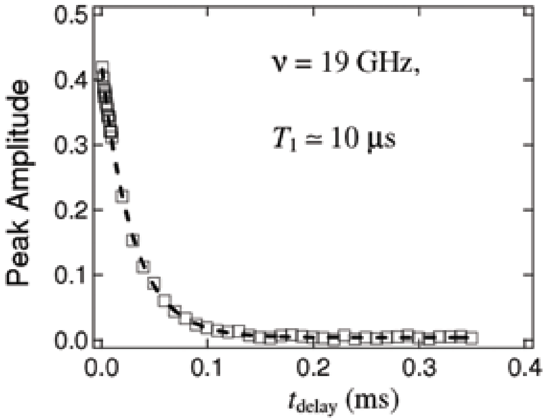

Figure 2: Normalized resonant peak amplitude as a function of readout delay time t_{delay}. The dashed line is the best fit to exponential decay with a time constant T_1 = 10 μs. The experimental data show remarkable agreement with the theory prediction.

REFERENCES:

[1] Yu, Y., D. Nakada, J. C. Lee, B. Singh, D. S. Crankshaw, T. P. Orlando, K. K. Berggren, W. D. Oliver, "Energy relaxation time between macroscopic quantum levels in a superconducting persistent-current qubit," *Physical Review Letters.*, vol. 92, no. 11, pp. 117904, March 2004.

[2] Yu, Y., W.D. Oliver, D. Nakada, J.C. Lee, K.K. Berggren, T.P .Orlando, "Energy relaxation times in a Nb persistent current qubit," submitted to *IEEE Transactions on AppliedSuperconductivity*, 2005.

Resonant Readout of a Persistent Current Qubit

J.C. Lee, W.D. Oliver, T.P. Orlando

Sponsorship: DURINT, ARDA, NSF

The two logical states of a persistent current (PC) qubit correspond to oppositely circulating currents in the qubit loop. The induced magnetic flux associated with the current either adds to or subtracts from the background flux. The state of the qubit can thus be detected by a DC superconducting quantum interference device (SQUID) magnetometer inductively coupled to the qubit. We have implemented a resonant technique that uses a SQUID as a flux-sensitive Josephson inductor for qubit readout. This approach keeps the readout SQUID biased at low currents along the supercurrent branch. Because the low bias reduces the level of decoherence on the qubit, it is more desirable for quantum computing applications. We also incorporated the SQUID inductor in a high-Q on-chip resonant circuit. This enabled us to distinguish the two flux states of a niobium PC qubit by observing a shift in the resonant frequency of the readout circuit. The nonlinear nature of the SQUID Josephson inductance, as well as its effect on the resonant spectra of the readout circuit, was also characterized.

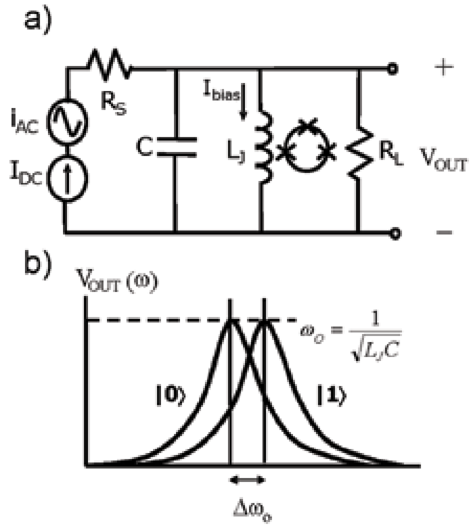

Figure 1: (a) The SQUID inductor is incorporated in a resonant readout circuit. It is inductively coupled to a PC qubit to detect its state. (b) A transition of the qubit state changes the Josephson inductance of the SQUID, and can be sensed as a shift in the resonant frequency of the readout circuit.

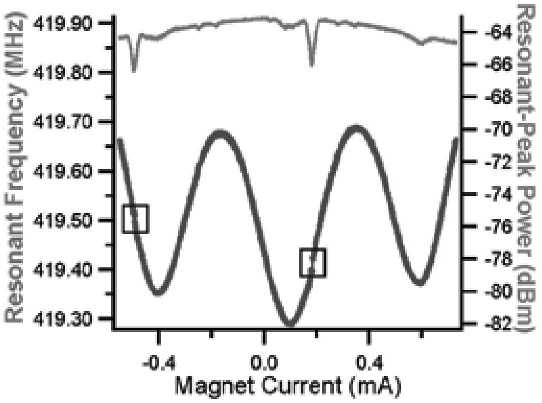

Figure 2: Experimental results at 300 mK: the lower plot (left axis) shows the modulation of the resonant frequency with external magnetic field. Qubit steps corresponding to transitions between opposite flux states were observed at every 1.3 periods of the SQUID lobe. The upper plot (right axis) shows the corresponding peak amplitude of the resonant spectrum. The dip in peak power coincides with the qubit step.

REFERENCES:

[1] Lee, J.C., W.D. Oliver, T.P. Orlando, “Resonant Readout of a Persistent Current Qubit,” *Applied Superconductivity Conference*, Jacksonville, FL, October 2004.

[2] Lee, J.C., “Magnetic Flux Measurement of Superconducting Qubits with Josephson Inductors,” Master’s Thesis, Massachusetts Institute of Technology, 2002.

Probing Decoherence with Electromagnetically Induced Transparency in Superconductive Quantum Circuits

K. Murali, W.Oliver, T.P. Orlando, in collaboration with Z. Dutton (Naval Research Laboratory)

Sponsorship: DURINT, ARDA

Superconductive quantum circuits (SQCs), comprising mesoscopic Josephson junctions, quantized flux, and/or charge states, are analogous to the quantized internal levels of an atom [1]. This SQC-atom analogy can be extended to the quantum optical effects associated with atoms, such as electromagnetically induced transparency (EIT) [2].

The three-level Λ-system for our S-EIT system (Figure1a) is a standard energy level structure utilized in atomic EIT. It comprises two meta-stable states |1⟩ and |2⟩, each of which may be coupled to a third excited state |3⟩. In an atomic EIT scheme, a strong "control" laser couples the |2⟩→|3⟩ transition, and a weak resonant "probe" laser couples the |1⟩→ |3⟩ transition. By itself, the probe laser light is readily absorbed by the atoms and thus the transmittance of the laser light through the atoms is very low. However, when the control and probe laser are applied simultaneously, destructive quantum interference between the atomic states involved in the two driven transitions causes the atom to become "transparent" to both the probe and control laser light [2,3,4]. Thus, the light passes through the atoms with virtually no absorption. In this work we propose to use EIT in SQCs to sensitively probe decoherence.

The SQC (Figure 1b) can be biased to result in an asymmetric double well potential as shown in Figure 2. The three states in the left well constitute the superconductive analog to the atomic Λ-system [5]. States |1⟩ and |2⟩ are "meta-stable" qubit states, with a tunneling and coherence time much longer than the excited "readout" state |3⟩. State |3⟩ has a strong inter-well transition when tuned on-resonance to state |4⟩. Thus, a particle reaching state |3⟩ will tend to tunnel quickly to state |4⟩, causing the circulating current to switch to the other direction, an event that is detected with a SQUID. Knowing how long the SQC remains transparent (i.e., does not reach state |3⟩) in the S-EIT experiment provides an estimate for decoherence time.

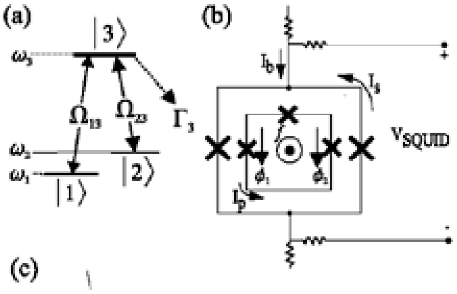

Figure 1: (a) Energy level diagram of a three-level Λ system. EIT can occur in atoms possessing two long-lived states |1>, |2>, each of which is coupled via resonant laser light fields to a radiatively decaying state |3>. (b) Circuit schematic of the persistent –current qubit and its readout SQUID.

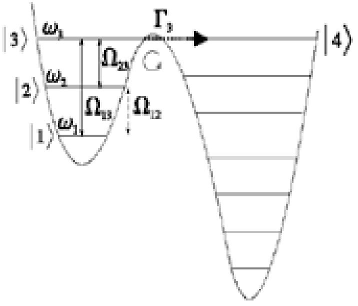

Figure 2: One-dimensional double-well potential and energy-level diagram for a three-level SQC.

REFERENCES:

[1] Leggett, A.J., A. Garg, "Quantum Mechanics versus Macroscopic Realism: Is The Flux There When Nobody Looks?" *Physical Review Letters*, vol. 54, no. 9, pp. 857-860, March 1985.

[2] Hau, L.V., S.E. Harris, Z. Dutton, C.H. Behroozi, "Light Speed Reduction to 17 Metres per Second in an Ultracold Atomic Gas," *Nature*, vol. 397, no. 6720, pp. 594-598, 1999.

[3] Boller, K.J., A. Imamoglu, S.E. Harris, "Observation of Electromagnetically Induced Transparency," *Physical Review Letters*, vol. 66, no. 20, pp. 2593-2596, May 1991.

[4] Cohen-Tannoudji, C., J. Dupont-Roc, G. Grynberg, Atom-photon intereactions, New York: John Wiley & Sons, Inc., 1992.

[5] Mooij, J.E., T.P. Orlando, L. Levitov, L. Tian, C.H. van der Wal, S. Lloyd, "Josephson Persistent-Current Qubit," *Science*, vol. 285, no. 5430, pp. 1036-1039, August 1999.

Type-II Quantum Computing Using Superconducting Qubits

D. Berns, W.M. Kaminsky, B. Cord, K.K. Berggren, W. Oliver, T.P. Orlando, in collaboration with
J. Yepez (Air Force Laboratories)

Sponsors: AFOSR, Fannie and John Hertz Foundation

Most algorithms designed for quantum computers will not best their classical counterparts until they are implemented with thousands of qubits. For example, the factoring of binary numbers with a quantum computer is estimated to be faster than a classical computer only when the length of the number is greater than about 500 digits [1]. In contrast, the Factorized Quantum Lattice-Gas Algorithm (FQLGA) [2] for fluid dynamics simulation, even when run on a quantum computer significantly smaller than the one just discussed, has significant advantages over its classical counterparts.

The FQLGA is the quantum version of classical lattice-gases (CLG)[3]. CLG are an extension of classical cellular automata with the goal of simulating fluid dynamics without reference to specific microscopic interactions. The binary nature of the CLG lattice variables is replaced for the FQLGA by the Hilbert space of a two-level quantum system. The results of this replacement are similar to that of the lattice-Boltzmann model, but with a couple of significant differences [4]. The first is the exponential decrease in required memory. The second is the ability to simulate arbitrarily small viscosities.

We have recently developed two implementations of the algorithm for the 1D diffusion equation using the PC qubit. The first consists of initializing the qubits while keeping them in their ground state, and then performing the collision by quickly changing their flux bias points and then performing a single $\pi/2$ pulse (Figure 1). This initialization technique could prove quite useful, since relaxation effects are avoided, but the way we have implemented the collision is not easily generalized to other collisions. A more general collision implementation was then developed by decomposing the unitary collision matrix into a sequence of single qubit rotations and coupled free evolution. The single qubit rotations then also serve to initialize the fluid's mass density.

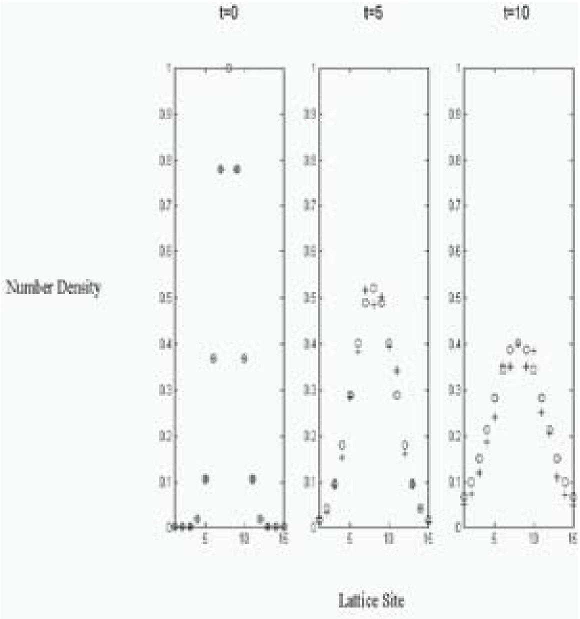

Figure 1: Simulation of the FQLGA for 1D diffusion is pictured(o) alongside simulation of the first proposed implementation(+). The expected diffusion of a gaussian is observed.

REFERENCES:

[1] K.K. Berggren, "Quantum Computing with Superconductors," *Proceedings of the IEEE*, vol. 92, no.10, pp. 1630-1638, October 2004.

[2] J. Yepez, "Quantum computation of Fluid Dynamics," *Lecture Notes in Computer Science*, vol. 1509, p. 34, February 1998.

[3] D.A. Wolf-Gladrow, "Lattice-Gas Cellular Automata and Lattice Boltzmann Models – An Introduction," (Berlin: Springer, 2000).

[4] J. Yepez, "An Efficient Quantum Algorithm for the One-Dimensional Burgers Equation," The Quantum Physics E-Print Archive, no. 0210092, October 2002; available at http://arxiv.org/archive/quant-ph.

Scalable Superconducting Architecture for Adiabatic Quantum Computation

W.M. Kaminsky, S. Lloyd, T.P. Orlando

Sponsorship: Fannie and John Hertz Foundation

Adiabatic quantum computation (AQC) is an approach to universal quantum computation in which the entire computation is performed in the ground state of a suitably chosen Hamiltonian [1]. As such, AQC offers intrinsic protection against dephasing and dissipation [2,3]. Moreover, AQC naturally suggests a novel quantum approach to the classically intractable constrained minimization problems of the complexity class NP. Namely, by exploiting the ability of coherent quantum systems to follow adiabatically the ground state of a slowly changing Hamiltonian, AQC promises to bypass automatically the many separated local minima occurring in difficult constrained minimization problems that are responsible for the inefficiency of classical minimization algorithms. To date, most research on AQC [4-8] has focused on determining the precise extent to which it could outperform classical minimization algorithms. The tantalizing possibility remains that---at least for all practical purposes---AQC offers at least a large polynomial, and often an exponential, speedup over classical algorithms. However, it may be the case that in the same way the efficiency of many practical classical algorithms for NP problems can only be established empirically, the efficiency of AQC on large instances of classically intractable problems can only be established by building a large-scale AQC experiment.

To make feasible such a large-scale AQC experiment, we have proposed a scalable architecture for AQC based on the superconducting persistent-current (PC) qubits [9,10] already under development here at MIT. As first proposed in [11], the architecture naturally incorporates the terms present in the PC qubit Hamiltonian by exploiting the isomorphism [12] between antiferromagnetic Ising models in applied magnetic fields and the canonical NP-complete graph theory problem Max Independent Set. Such a design notably removes any need for the interqubit couplings to be varied during the computation. Moreover, since Max Independent Set remains NP-complete even when restricted to planar graphs where each vertex is connected to no more than 3 others by edges, a scalable programmable architecture capable of posing any problem in the class NP may simply take the form of a 2D, hexagonal, square, or triangular lattice of qubits. Finally, the latest version of the architecture [13] permits interqubit couplings to be limited to nearest-neighbors and qubit measurements to be inefficient.

REFERENCES:

[1] Aharonov, D., W. van Dam, J. Kempe, Z. Landau, S. Lloyd, O. Regev, “Adiabatic Quantum Computation is Equivalent to Standard Quantum Computation,” *The Quantum Physics E-Print Archive*, no. 0405098, March 2005; available: http://arxiv.org/abs/quant-ph/0405098.

[2] Childs, A.M., E. Farhi, J. Preskill, “Robustness of Adiabatic Quantum Computation,” *Physical Review A: Atomic, Molecular, and Optical Physics*, vol. 65, no. 1, pp. 012322: 1-10, January 2002.

[3] Roland, J., N.J. Cerf, “Noise Resistance of Adiabatic Quantum Computation Using Random Matrix Theory,” *Physical Review A: Atomic, Molecular, and Optical Physics*, vol. 71, no. 3, p. 032330: 1-9, March 2005.

[4] Farhi, E., J. Goldstone, S. Gutmann, J. Lapan, A. Lundgren, D. Preda, “A Quantum Adiabatic Evolution Algorithm Applied to Random Instances of an NP-complete problem,” *Science*, vol. 292, pp. 472-475, April 2001.

[5] Childs, A.M., E. Farhi, J. Goldstone, S. Gutmann, “Finding Cliques by Quantum Adiabatic Evolution,” *Quantum Information and Computation*, vol. 2, no. 3, pp. 181-191, May 2002.

[6] van Dam, W., M. Mosca, U. Vazirani, “How Powerful is Adiabatic Quantum Computation?” *42nd Annual Symposium on Foundations of Computer Science,* Las Vegas, NV, pp. 279–287, October 2001.

[7] Farhi, E., J. Goldstone, S. Gutmann, “Quantum Adiabatic Evolution Algorithms versus Simulated Annealing,” *The Quantum Physics E-Print Archive*, no. 0201031, January 2002; available: http://arxiv.org/abs/quant-ph/0201031.

[8] Santoro, G.E. *et al.*, “Theory of Quantum Annealing of an Ising Spin Glass,” *Science*, vol. 295, pp. 2427-2430, March 2002.

[9] Mooij, J.E. *et al.*, “Josephson persistent-current qubit,” *Science*, vol. 285, pp. 1036-1039, August 1999.

[10] Orlando, T.P. *et al.* “Superconducting Persistent-current Qubit,” *Physical Review B: Condensed Matter and Materials Physics*, vol. 60, no. 22, pp. 15398-15413, December 1999.

[11] Kaminsky, W.M., S. Lloyd, “Scalable Architecture for Adiabatic Quantum Computing of NP-hard Problems,” in *Quantum Computing and Quantum Bits in Mesoscopic Systems*, ed. A.J. Leggett, B. Ruggiero, P. Silvestrini, (New York: Kluwer Academic, 2004), pp. 229-236.

[12] Barahona, F., “On the Computational Complexity of Ising Spin Glass Models,” *Journal of Physics A: Mathematical and General*, vol. 15, no. 10, pp. 3241-3253, October 1982.

[13] Kaminsky, W.M., S. Lloyd, T.P. Orlando, “Scalable Superconducting Architecture for Adiabatic Quantum Computation,” *The Quantum Physics E-Print Archive*, no. 0403090, March 2004; available: http://arxiv.org/abs/quant-ph/0403090.